A Section 508–conformant HTML version of this article is available at https://doi.org/10.1289/EHP9413.

Effect of Atmospheric Aging on Soot Particle Toxicity in Lung Cell Models at the Air–Liquid Interface: Differential Toxicological Impacts of Biogenic and Anthropogenic Secondary Organic Aerosols (SOAs)

Svenja Offer,[1,2] Elena Hartner,[1,2] Sebastiano Di Bucchianico,[1] Christoph Bisig,[1] Stefanie Bauer,[1] Jana Pantzke,[1,2] Elias J. Zimmermann,[1,2] Xin Cao,[1,2] Stefanie Binder,[1,2] Evelyn Kuhn,[1] Anja Huber,[1] Seongho Jeong,[1,2] Uwe Käfer,[1,2] Patrick Martens,[2] Arunas Mesceriakovas,[3] Jan Bendl,[1,4,5] Ramona Brejcha,[1] Angela Buchholz,[6] Daniella Gat,[7] Thorsten Hohaus,[8] Narges Rastak,[1] Gert Jakobi,[1] Markus Kalberer,[9] Tamara Kanashova,[10] Yue Hu,[11] Christoph Ogris,[11] Annalisa Marsico,[11] Fabian Theis,[11] Michal Pardo,[7] Thomas Gröger,[1] Sebastian Oeder,[1] Jürgen Orasche,[1] Andreas Paul,[8] Till Ziehm,[8] Zhi-Hui Zhang,[9] Thomas Adam,[1,4] Olli Sippula,[3] Martin Sklorz,[1] Jürgen Schnelle-Kreis,[1] Hendryk Czech,[1,2] Astrid Kiendler-Scharr,[8] Yinon Rudich,[7] and Ralf Zimmermann[1,2]

[1]Joint Mass Spectrometry Center (JMSC) at Comprehensive Molecular Analytics, Helmholtz Zentrum München, Neuherberg, Germany
[2]JMSC at Analytical Chemistry, Institute of Chemistry, University of Rostock, Rostock, Germany
[3]Department of Environmental and Biological Sciences, University of Eastern Finland, Kuopio, Finland
[4]Institute for Chemistry and Environmental Engineering, University of the Bundeswehr Munich, Neubiberg, Germany
[5]Institute for Environmental Studies, Faculty of Science, Charles University, Prague, Czech Republic
[6]Department of Applied Physics, University of Eastern Finland, Kuopio, Finland
[7]Department of Earth and Planetary Sciences, Faculty of Chemistry, Weizmann Institute of Science, Rehovot, Israel
[8]Institute of Energy and Climate Research, Troposphere, Forschungszentrum Jülich GmbH, Jülich, Germany
[9]Department of Environmental Sciences, University of Basel, Basel, Switzerland
[10]Max-Delbrück-Centrum für Molekulare Medizin, Berlin, Germany
[11]Institute of Computational Biology, Helmholtz Zentrum München, Neuherberg, Germany

Background: Secondary organic aerosols (SOAs) formed from anthropogenic or biogenic gaseous precursors in the atmosphere substantially contribute to the ambient fine particulate matter [PM ≤2.5 μm in aerodynamic diameter ($PM_{2.5}$)] burden, which has been associated with adverse human health effects. However, there is only limited evidence on their differential toxicological impact.

Objectives: We aimed to discriminate toxicological effects of aerosols generated by atmospheric aging on combustion soot particles (SPs) of gaseous biogenic (β-pinene) or anthropogenic (naphthalene) precursors in two different lung cell models exposed at the air–liquid interface (ALI).

Methods: Mono- or cocultures of lung epithelial cells (A549) and endothelial cells (EA.hy926) were exposed at the ALI for 4 h to different aerosol concentrations of a photochemically aged mixture of primary combustion SP and β-pinene ($SOA_{\beta PIN}$-SP) or naphthalene (SOA_{NAP}-SP). The internally mixed soot/SOA particles were comprehensively characterized in terms of their physical and chemical properties. We conducted toxicity tests to determine cytotoxicity, intracellular oxidative stress, primary and secondary genotoxicity, as well as inflammatory and angiogenic effects.

Results: We observed considerable toxicity-related outcomes in cells treated with either SOA type. Greater adverse effects were measured for SOA_{NAP}-SP compared with $SOA_{\beta PIN}$-SP in both cell models, whereas the nano-sized soot cores alone showed only minor effects. At the functional level, we found that SOA_{NAP}-SP augmented the secretion of malondialdehyde and interleukin-8 and may have induced the activation of endothelial cells in the coculture system. This activation was confirmed by comet assay, suggesting secondary genotoxicity and greater angiogenic potential. Chemical characterization of PM revealed distinct qualitative differences in the composition of the two secondary aerosol types.

Discussion: In this study using A549 and EA.hy926 cells exposed at ALI, SOA compounds had greater toxicity than primary SPs. Photochemical aging of naphthalene was associated with the formation of more oxidized, more aromatic SOAs with a higher oxidative potential and toxicity compared with β-pinene. Thus, we conclude that the influence of atmospheric chemistry on the chemical PM composition plays a crucial role for the adverse health outcome of emissions. https://doi.org/10.1289/EHP9413

Introduction

Over the past decades, the impact of ambient fine particulate matter [PM ≤2.5 μm ($PM_{2.5}$)] on the global burden of disease has gained substantial attention. Epidemiological cohort studies have found significant correlations between the exposure to $PM_{2.5}$ and substantial effects on human health, such as respiratory and cardiovascular diseases, and increased morbidity and mortality (Brook et al. 2010; Cohen et al. 2017; Pope et al. 2020). It is well accepted that the toxicity of $PM_{2.5}$ varies between its sources and formation pathways. However, it is still largely unknown which PM properties—such as size, mass, shape, surface properties, or chemical composition—induce biological responses (Burkholder et al. 2017; Park et al. 2018; Wyzga and Rohr 2015). Furthermore, our knowledge is mostly limited to the effects of collected airborne particles under submerged exposure conditions rather than the direct deposition and interaction of aerosols with cell cultures (Ihantola et al. 2020; Oeder et al. 2015). Submerged exposures do not reflect the physiological condition of airway barriers because inhalation occurs by aerosol deposition onto airway epithelial cells that form, together with, for example, endothelial cells and basal membranes, a tissue layer enabling gas exchanges between the lungs and the blood circulation (Barosova et al. 2021). Air–liquid interface (ALI) aerosol exposures offer several advantages compared with submerged conditions. These include the preservation of the physicochemical characteristics of airborne PM and a higher sensitivity both in terms of effective doses, which are lower at the ALI, and in terms of transcripts regulation and protein enrichment, which are more pronounced in alveolar epithelial A549 cells

Address correspondence to Sebastiano Di Bucchianico, Joint Mass Spectrometry Center at Comprehensive Molecular Analytics, Helmholtz Zentrum München, Ingolstädter Landstr. 1, D-85764 Neuherberg, Germany. Email: dibucchianico@helmholtz-muenchen.de

Supplemental Material is available online (https://doi.org/10.1289/EHP9413).

All authors declare they have no actual or potential competing financial interests.

Received 31 March 2021; Revised 17 December 2021; Accepted 22 December 2021; Published 3 February 2022.

exposed at ALI compared with submerged exposures (Hilton et al. 2019; Lenz et al. 2013; Loret et al. 2016). It has been shown that ALI-cultured A549 cells retain more of the usual patterns of tight junction proteins, such as occluding, claudin-2, and zonula occludens-3, as well as show lower permeation coefficient values than the submerged cells, resulting in a clear and tighter epithelial phenotype (Rothen-Rutishauser et al. 2008).

Atmospheric aerosol particles may originate from primary sources (primary aerosols), but they are also formed and altered by oxidative gas-to-particle conversion in the atmosphere (secondary aerosols) as well as complex multiphase chemistry (aged primary aerosols) (Hallquist et al. 2009). The sources contributing to the global primary aerosol load are manifold and from both anthropogenic and natural origin, including industrial processes, traffic, sea spray, and wildfire burnings. Soot, or its related entities black carbon (BC) and elemental carbon (EC), is released from both anthropogenic (e.g., traffic, residential heating, industry) and naturally occurring (e.g., wildfire) combustion processes (Bond et al. 2013). In contrast to BC and EC, the term soot particles (SPs) is less specific and does not refer to carbon atoms only. Instead, it is described as black particles that can enter the atmosphere through combustion processes (Andreae and Gelencsér 2006), so it also includes organic and inorganic PM. SP has impacts on human health upon inhalation (Janssen et al. 2011); however, freshly emitted SP become very quickly coated by secondary aerosols in ambient air (Moore et al. 2014). Secondary aerosols are generated from volatile precursors by atmospheric oxidants, such as hydroxyl (OH), ozone (O_3), and nitrate radicals, or by photolysis in the atmosphere (Hallquist et al. 2009; Shakya and Griffin 2010). Secondary organic aerosols (SOAs) from the oxidative conversion of volatile organic compounds (VOCs) may increase levels of ambient $PM_{2.5}$ considerably, causing severe haze pollution episodes (Huang et al. 2014). Naphthalene and β-pinene were found to be substantial contributors to the anthropogenic (Jia and Batterman 2010) and biogenic (Guenther et al. 2012) global VOC emissions, respectively, with significant potential to form SOAs (Chen et al. 2016; Watne et al. 2017).

Naphthalene represents the smallest and most volatile polycyclic aromatic hydrocarbon (PAH) and is classified by the International Agency for Research on Cancer as probably carcinogenic to humans (Group 2B) (IARC 2010). It is mainly formed during combustion processes, such as fossil fuel combustion in engines, in particular diesel engines, biomass burning, or tobacco smoking, as well as in the chemical and metal industries (Jia and Batterman 2010; Qian et al. 2021; Wang et al. 2020). Because of its high vapor pressure, naphthalene is mainly in the gas phase at ambient conditions and thus undergoes homogeneous gas-phase reactions in the atmosphere, which can result in products of lower volatility accompanied with their conversion into the particle phase and the generation of SOAs (Williams et al. 2010). β-pinene is a monoterpene, one of the main compounds released by vegetation, such as by various coniferous plants (Faiola et al. 2015; Kleist et al. 2012). Its oxidation leads to substantial yields of SOAs (Sarrafzadeh et al. 2016; Xavier et al. 2019), including the formation of highly oxidized extremely low-VOCs (Ehn et al. 2014). On a global scale, biogenic VOCs largely exceed the emissions of anthropogenic VOCs; however, anthropogenic VOCs may regionally reach higher levels than biogenic VOCs (Guenther et al. 1995). In the case of biogenic VOCs (isoprene, terpenes) toxicity is generally enhanced by photochemical aging; however, there is an unambiguous effect of aging for PAHs and engine emissions (Weitekamp et al. 2020; Xu et al. 2022).

Depending on the size of the PM, their retention in the lung varies. Although inhaled particles between 5 and 10 μm in aerodynamic diameter typically affect only the upper airways and are removed by mucociliar clearance, particles in the range between 1 and 2.5 μm are able to penetrate deep into the respiratory regions and particles <1 μm can easily deposit on alveoli and be retained in the surfactant (Heyder 2004). Moreover, an *in vivo* study showed that not only can ultrafine PM [PM ≤ 0.1 μm ($PM_{0.1}$)] enter extrapulmonary organs, but particles with an aerodynamic diameter of between 0.2 and 2 μm can also (Li et al. 2019). In addition to the direct harm of particles to the organs, several *in vitro* studies in human lung epithelial cells have shown that the $PM_{2.5}$ of SOA can trigger inflammation with systemic effects through the release of pro-inflammatory cytokines (Feng et al. 2016), an increase in reactive oxygen species (ROS) (Arashiro et al. 2018), and an impairment of the anti-oxidant system (Arashiro et al. 2018; Deng et al. 2013; Kouassi et al. 2010; Longhin et al. 2013). In response, oxidative stress further triggers inflammatory and mutagenic responses (Dergham et al. 2012; Lin et al. 2017; Longhin et al. 2013; Møller et al. 2014; Riediker et al. 2019). Beyond the size of ambient $PM_{2.5}$, its chemical composition is assumed to play an important role in the toxicity of the particles (Eaves et al. 2020; Sýkorová et al. 2016). Oxidation flow reactor (OFR) studies have revealed a greater toxic effect of higher photochemically aged α-pinene- and naphthalene-derived SOAs on A549 cells compared with their SOAs of lower photochemical age, which was attributed to the increased formation of ROS (Chowdhury et al. 2018, 2019).

Within the project aeroHEALTH (https://www.aerohealth.eu), the present study aimed to investigate the toxicological impacts of two model systems representing air pollution by primary combustion emissions (e.g., SPs) and atmospheric processing of a typical anthropogenic (e.g., naphthalene) or biogenic (e.g., β-pinene) VOC precursor. In the used experimental setup, the SOAs were generated in an OFR in the presence of freshly formed combustion soot, leading to coating SPs with condensed organic matter from naphthalene (SOA_{NAP}-SP) and β-pinene ($SOA_{\beta PIN}$-SP), respectively. Two different cell culture systems were exposed to these aerosols at the ALI. Increasing epidemiological and experimental evidences show that environmental exposure may disturb airway intercellular communication by indirect mechanisms, such as the release of inflammatory cytokines, or by direct mechanisms, including particles translocating from the lung into the circulation (Peters et al. 2021; Wang et al. 2019). Especially in the alveolar region, PAHs contained in the gas phase or detached from the particle surface may be displaced across the airway barriers and reach cells and secondary tissues that are not directly exposed (Låg et al. 2020). In view of the important role of these mechanisms, A549 human alveolar epithelial cells were grown either as a monoculture on an insert membrane or as a coculture model with microvascular endothelial EA.hy926 cells on the basolateral side of the membrane to mimic the blood–air barrier and to evaluate cell-to-cell interplay. We performed assays testing for aerosol-induced oxidative stress, inflammation, geno- and cytotoxicity, as well as to elucidate possible secondary effects derived from cellular interplay, according to adverse outcome pathways (Halappanavar et al. 2020). With this setup, we aimed to address the overarching scientific question whether atmospheric aging and the related formation and condensation of SOAs on SPs can increase the toxicity of the particles and whether the SOA precursor plays a decisive role in the biological response.

Material and Methods

Aerosol Generation and Characterization

Aerosol generation and sampling setup. SOAs of either naphthalene (Sigma-Aldrich; 147141-25G; 99%) or β-pinene (Sigma-Aldrich; 402753-10G; ≥99 %) were produced by mixing their pure vapor with SPs and subsequent processing in an OFR [i.e., a

potential aerosol mass (PAM) reactor] (Bruns et al. 2015; Kang et al. 2007) for the simulation of atmospheric photooxidation (aging) by OH radicals. In addition, pure SPs were also fed into the PAM reactor without aging and used as the reference control. This was done because SPs and SOA precursors refer to primary compounds, which are simultaneously transformed by atmospheric aging. However, SOA rapidly starts to cover the surface of the SPs, and the particle constitution may be described by a core–shell model. Only particulate organic species at or near the particle surface are exposed to OH radicals, whereas the soot core of the particle is shielded against heterogeneous oxidation (Lim et al. 2017). Considering the generally slower reaction kinetics of heterogeneous oxidation compared with the homogeneous oxidation involved in SOA formation, we may assume that soot cores are oxidized to a negligible extent. Therefore, fresh SPs, rather than aged SPs, without the addition of SOA precursors were used as the reference. A simplified scheme of the setup is shown in Figure 1.

First, SPs, functioning as a condensation sink for SOAs, were produced by a CAST-Burner (Combustion Aerosol Standard; model 5201C; Jing) under lean combustion conditions (50 mL/min propane, 0 mL/min MixN_2, 1.42 L/min Oxid.Air, and 20 L/min Dil. Air) to minimize the organic content and generate EC-rich particles with a Gaussian size distribution (geometric mean $\sim$100 nm). A custom-made porous tube diluter with a variable mass flow-controlled dilution ratio was applied as a first dilution step. Naphthalene or β-pinene vapors were produced using a custom-made diffusion source, placed in a temperature-controlled water bath, using nitrogen (99.999% purity) with a flow rate of 1 L/min. The length and diameter of the diffusion source, as well as the bath temperature, were adjusted for each VOC individually to maintain the same precursor concentration. The bath temperatures for VOC generation were $\sim$40°C for β-pinene and $\sim$60°C for naphthalene. Diameters of the diffusion source were 10 mm for β-pinene (length 40 mm) and 25 mm for naphthalene (length $\sim$5 mm), with an additional 25 mm of frit to prevent turbulent mixing and reduce diffusion. The targeted VOC concentration of 4 mg/m^3 was adjusted every day before the experiment and verified after the experiment by a flame ionization detector (model 109A; J.U.M. Engineering). The mixture of soot and VOC was humidified during a second dilution step using an ejector diluter (Palas VKL 10; Palas GmbH) with a fixed 1:10 dilution ratio. Here, humidified air (moistened by a PermaPure humidifier FC125-240; Perma Pure), mixed with 0.3 mL/min nitrogen, containing deuterated butanol (D9-butanol; 98% isotopic purity; Sigma Aldrich) was used as dilution medium. Final concentrations entering the PAM reactor were 1 mg/m^3 soot, 4 mg/m^3 VOC, and 80 ppbV D9-butanol at 40% relative humidity (RH).

The PAM reactor (Bruns et al. 2015; Kang et al. 2007) refers to an OFR with an internal volume of 15 L and was operated at a flow rate of 8 L/min, resulting in a mean residence time of 113 s. It generates O_3 *in situ* and, subsequently, OH radicals from irradiating humid air by two ultraviolet (UV)-lamps (BHK Inc.) with emission

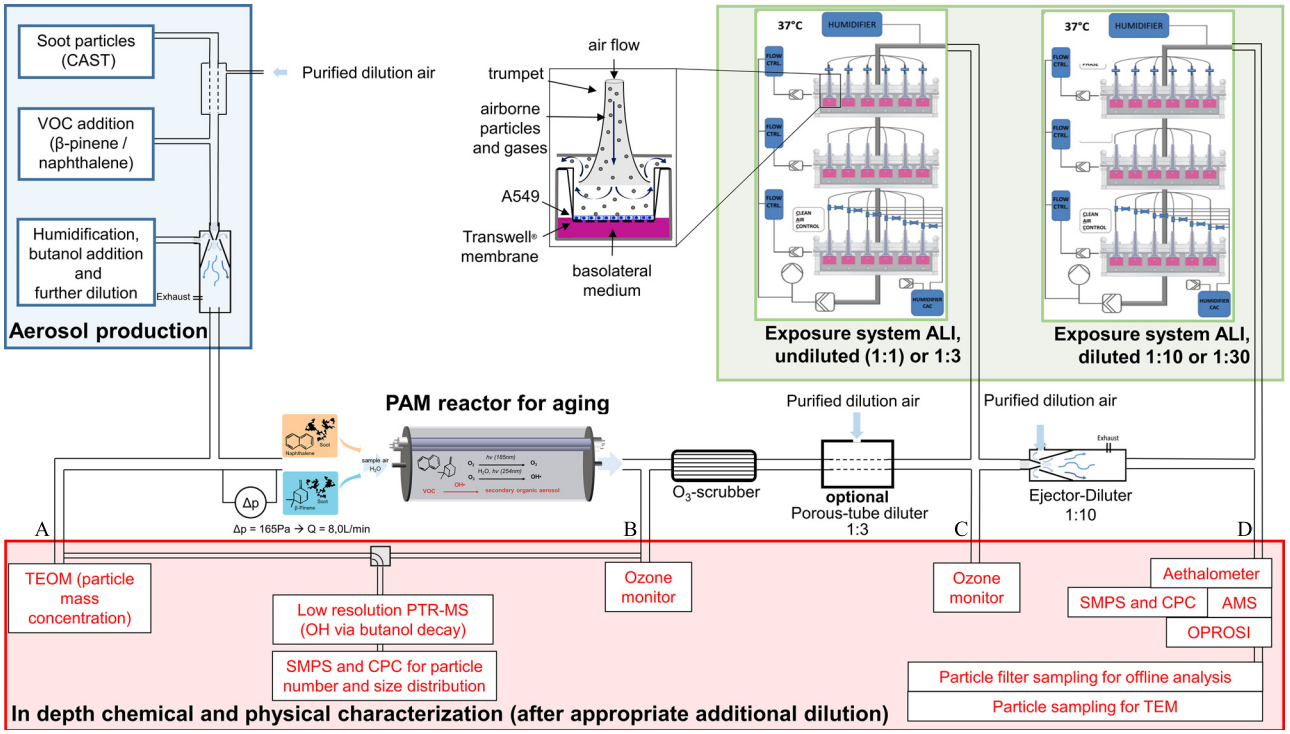

Figure 1. A schematic overview of the aerosol generation, sampling method, and ALI exposure system. SP (CAST soot; 1 mg/m^3) together with either β-pinene (4 mg/m^3) or naphthalene (4 mg/m^3) passed through a PAM reactor for photochemical aging by OH radicals after humidification and appropriate dilution. In addition, pure SP (CAST soot; 1 mg/m^3) were fed into the PAM reactor without aging and used as the reference control. O_3, which was produced *in situ* by the PAM reactor, was removed after the reactor by an O_3-scrubber to a level <10 ppb. State-of-the-art methods characterized the chemical and physical properties of the generated SOA [line A: TEOM; line A/B: PTR-MS, SMPS, CPC, O_3 monitor; line C: O_3 monitor; line D: Aethalometer, SMPS, AMS, OPROSI, offline sampling (VOC adsorber, TEM, GC × GC-TOFMS)]. Two ALI exposure systems were used in parallel. An optional 1:3 diluter in front of one ALI exposure system and a 1:10 diluter in front of the second ALI exposure system were applied to investigate different dilutions of the aerosol [undiluted (1:1), 1:3, 1:10, and 1:30]. The magnification of a single exposure position illustrates the air flow of the aerosol over the cells growing on the membrane of Transwell inserts and shows aerosol deposition by diffusion. Note: ALI, air-liquid interface; AMS, high-resolution time-of-flight aerosol mass spectrometer; CAST, combustion aerosol standard; CPC, condensation particle counter; Δp, change in pressure; GC × GC-TOFMS, comprehensive two-dimensional gas chromatography–time-of-flight mass spectrometer; OH, hydroxy; OPROSI, online particle-bound ROS (reactive oxygen species) instrument; ozone, O_3; PAM, potential aerosol mass; PTR-MS, quadrupole proton–transfer reaction mass spectrometer; SMPS, scanning mobility particle sizer; SOA, secondary organic aerosol; SP, soot particle; TEM, Transmission electron microscope; TEOM, tapered element oscillating microbalance; VOC, volatile organic compounds.

lines at 185 and 254 nm. We adjusted the UV lamp power to obtain similar photochemical ages (~ 3 d) of both types of SOAs, accounting for the different rate constants of naphthalene and β-pinene toward the OH radical (k_{OH} (naphthalene) $= 2.3 \times 10^{-11}$ s/cm^3; k_{OH} (β-pinene) $= 7.4 \times 10^{-11}$ s/cm^3 (Atkinson and Arey 2003). Although SOA-precursors and SP were exposed to O_3 concentrations of 6.0 ± 0.6 ppm (β-pinene) and 5.4 ± 0.3 ppm (naphthalene) for 113 s, the aging under the described conditions is strongly dominated by OH radical chemistry (Atkinson and Carter 1984; Sarrafzadeh et al. 2016). Fractional importance of non-OH fate, including photolysis at 185 and 254 nm, as well as reactions with $O(^1D)$, $O(^3P)$, and O_3, were found to be comparable to ambient air assessed by the PAM model of Peng et al. (2016). Furthermore, the surface oxidation of SP by O_3 is estimated to be negligible based on the kinetic data of Chughtai et al. (2003).

A ceramic honeycomb denuder, impregnated with sodium nitrite was installed downstream of the PAM reactor to remove O_3 to a level of <10 ppbV, and monitored by the O_3 monitor. In addition, a custom-made porous tube diluter (fixed at a 1:3 dilution) and an ejector diluter (1:10 dilution) (Palas) were installed in the sampling lines guided to the two ALI exposure systems to obtain the different dilution ratios [undiluted (1:1), 1:3, 1:10, and 1:30] for the cell exposures. All dilution steps were conducted with purified compressed laboratory air, compressed by an oil-free compressor (SF4; Atlas Copco) and purified by a modified catalytic converter (737-15; Aadco), which removed hydrocarbons, including methane, to a concentration of <10 ppbV.

Online aerosol measurements. Four sampling points were used for the online aerosol measurements (Figure 1). A detailed description of the respective methods are outlined in the below paragraphs.

Particle number and particle size distribution. A scanning mobility particle sizer (SMPS) comprised of an electrostatic classifier (TSI; model 3082) connected to a condensation particle counter (TSI; model 3750) was installed at line D. Multiple charge correction and diffusion loss correction were done using AIM software (version 10.3; TSI). A second electrostatic classifier (TSI; model 3082) connected to a 3025A CPC (TSI) was installed with the option to switch between line A or line B without additional dilution for monitoring the feed and aged aerosol properties.

BC and particle mass. A seven-wavelength aethalometer (model Magee AE33; Aerosol d.o.o.) was used at line D to confirm stable SP concentrations, measured as BC at 880 nm, whereas the difference of the PM concentration at 370 and 880 nm, denoted as brown carbon (BrC), confirmed the stable formation of SOA over the whole cell exposure time. In addition, a tapered element oscillating microbalance (TEOM 1400a; Rupprecht & Patashnick Co., Inc.) was used to determine the SP mass concentration at line A. Both instruments had own ejector diluters (1:10 dilution) (Palas), ensuring the appropriate concentrations.

Photochemical age. D9-butanol was used as a photochemical clock and was measured before and after the PAM reactor step by a quadrupole proton–transfer reaction mass spectrometer (PTR-MS; Ionicon). With a rate constant of 3.4×10^{-12} cm^3/s for D9-butanol and a mean PAM reactor residence time of 112.5 s, the OH radical exposure can be calculated and subsequently converted into an equivalent photochemical age (Barmet et al. 2012), assuming an average ambient OH radical concentration of 10^6 molecules/cm^3 (Prinn et al. 2001). The PTR-MS was installed in parallel to the second electrostatic classifier (switching between line A and line B) and setup in multiple ion detection mode, with an estimated detection limit of 0.5 ppb. For experiments with naphthalene: *m/z* 21 (primary water ion, $[H_2{}^{18}O+H]^+$), 66 (D9-butanol fragment $[M\text{-}HDO+H]^+$), 129 (naphthalene $C_{10}H_8$, $[M+H]^+$, for quantification), and 159 (naphthoquinone $C_{10}H_6O_2$, $[M+H]^+$) were recorded. For experiments with β-pinene: *m/z* 21, 66, 137 (β-pinene $[M+H]^+$, for quantification), and 81 (β-pinene fragment $[M\text{-}C_4H_6+H]^+$, as qualifier).

O_3, which was formed *in situ* by vacuum ultraviolet (VUV) radiation at 185 nm, was quantified after a 10-fold dilution with pure nitrogen by an O_3 monitor (model O_3 41 M; Environment S. A./Ansyco GmbH) at line B. A second O_3 monitor (model APOA 350E; Horiba) was installed at line C to guarantee that no O_3 reached the ALI systems.

Elemental ratios. A high-resolution time-of-flight aerosol mass spectrometer (AMS; Aerodyne Inc.) (DeCarlo et al. 2006) was operated at line D to determine ratios of the elements O/C and H/C, the total mass concentration, and a size distribution of the nonrefractory organic chemical composition. The instrument was run with a vaporizer temperature of 560°C, with an averaging time of 4 min. The resulting mass spectrum was analyzed in the *m/z* range of 12–220 amu because the fractions >200 amu have little to no impact on the total organic concentration or the elemental composition, given that we observed no $m/z > 200$ amu. Calibrations were preformed weekly using dried 350-nm ammonium nitrate particles, size selected based on mobility diameter with a differential mobility analyzer and a condensation particle counter (TSI; model 3786), as described previously (Jayne et al. 2000). The ionization efficiency was found to be 7.0×10^{-8} before experiments and 6.0×10^{-8} after the experiments. The collection efficiency, used to correct for nonunity collection, was calculated as the percentage of organics detected by the AMS compared with the CPC, assuming a density of 1.4 mg/m^3, and was found to be $\sim 70\%$. The method used to analyze the elemental composition of the aerosol is described in detail elsewhere (Canagaratna et al. 2015).

ROS measurement. An online particle-bound ROS instrument (OPROSI; University of Basel) was installed on line D with an 10-fold ejector diluter (Palas) to trace the oxidative potential as described previously by Wragg et al. (2016). The occurrence of ROS is based on H_2O_2 measurements.

Offline aerosol measurements. In parallel to the online chemical and physical characterization, $PM_{2.5}$ particles were sampled on prebaked (500°C) quartz fiber (QF) filters (Pall Corporation; Tissuquartz) for offline chemical characterization. Filters with a total sampling volume of 600 L were collected either at a 10-L/min flow rate (60 min collection time) or at a 5-L/min flow rate (120 min collection time), respectively.

Particulate carbon and chemical SOA composition. EC and organic carbon (OC) were determined from the QF filters using a thermal-optical carbon analyzer (Desert Research Institute model 2001A; Atmoslytic Inc.) following the IMPROVE_A protocol (Chow et al. 2007). The chemical SOA composition was investigated with two complementary MS techniques from particles collected on filters as described above: Direct inlet probe–high-resolution time-of-flight mass spectrometer (DIP-HRTOFMS; Pegasus GC-HRT 4D; LECO) (Käfer et al. 2019) and comprehensive two-dimensional gas chromatography (GC × GC)–TOFMS; Pegasus BT 4D GC × GC; LECO) with thermal desorption (TD). For DIP-HRTOFMS, round filter punches with a diameter of 2 mm were analyzed by TD in the ion source (40°C −2/s −400°C) in four replicates. Raw spectra were blank corrected, summed over the whole run, and found ions were assigned to elemental formulas limited to 1–50 carbon, 0–102 hydrogen, and 0–5 oxygen atoms within a relative mass error window of 5 ppm. Last, ions with odd nominal mass, which represent fragments from the electron ionization, were removed from the data set to focus on molecular ions. The TD-GC × GC-TOFMS was operated with an OPTIC-4 GC inlet system (GL Sciences), with helium (Helium 5.0; Linde AG) as the carrier gas and a GC column set consisting of an SGE BPX5 capillary column [5% phenyl polysilphenylene–siloxane, 60 m,

0.25 mm internal diameter (i.d.), 0.25 μm film thickness (df); SGE] in the first dimension (1D) and an SGE BPX50 capillary column [50% phenyl polysilphenylene–siloxane, 1.5 m, 0.1 mm i.d., 0.1 μm df; SGE] in the second dimension (2D). The desorbed semivolatile organic compounds (SVOCs) were cryogenically focused via the cryogenic trapping system Cryofocus-4 (GL Sciences) at −100°C using liquid nitrogen. The temperature for TD in the OPTIC-4 inlet system was gradually ramped at 2°C/s from 40°C to 300°C to gently introduce aerosol particle constituents onto the GC column with reduced thermal fragmentation. The inlet purge time was 100 s at a column flow of 1 mL/min and a split flow of 100 mL/min. The desorption flow rate was 2.6 mL/min in spitless mode. After TD, the column flow was adjusted to 1 mL/min, and the split flow to 100 mL/min, for the remainder of the measurement. After 10 min of holding the initial temperature of 40°C in the primary oven, it was ramped at 2°C/min from 40°C to 250°C, after which a gradient of 5°C/min was applied to 330°C and held for 10 min. The secondary oven was offset by +20 °C from the primary oven, and the modulator temperature was offset by 15°C to the secondary oven temperature. The modulation period was 5 s, with a hot pulse time of 1.5 s. The MS transfer line temperature was set to 300°C. Mass acquisition was done from 20 to 700 Da at 100 spectra/s. The electron energy was 70 eV, and the ion source temperature was 250°C. Data acquisition and processing was carried out using the ChromaTOF software (version 5.5; LECO). Postprocessing was done with a minimum peak signal-to-noise value (S/N) of 1,000, which resulted in a total peak number of 397 and 798 peaks for SOA_{NAP}-SP and $SOA_{\beta PIN}$-SP, respectively.

Transmission electron microscopy (TEM) images. Were taken for selected experiments by guiding a small volume (100 mL/min) of the aerosol flow for 2–10 min through a carbon sampling grid (400 mesh copper; Agar Scientific). Sampled grids were stored at room temperature (RT) at low humidity in a desiccator prior to analysis using a TEM (JEM-2100F; JEOL Ltd) at 200 kV.

ALI Exposure Systems and Cell Culture

ALI exposure. Two custom-made automated exposure systems (Vitrocell Systems) were used to expose cells at ALI at different dilutions of the aerosols [undiluted (1:1), 1:3, 1:10, and 1:30]. The tested aerosol was guided through a size-selective impactor that excluded particles with size fractions $>PM_{10}$, before entering the inlet of the ALI exposure system and the main reactor. The ALI exposure systems were operated with different settings compared with previous publications (Mülhopt et al. 2016; Oeder et al. 2015). The total aerosol flow (inlet) was reduced to 5 L/min owing to the limited aerosol flow through the PAM reactor. The cabinet was heated to a temperature of 39.4°C to reduce water condensation in the tubes. Both systems comprised three Vitrocell 6/6 CF Stainless modules, thus enabling the exposure of six inserts of a 6-well format per module. Every position in the module was supplied with separate air flow over a trumpet taken from the main reactor. Exposure to the tested aerosol was conducted in 12 positions per ALI exposure system, in which the aerosol was passed over the cells growing on Transwell inserts and deposition was controlled only by diffusion. A simplified scheme of the setup is shown in Figure 1. In addition to the aerosol exposures, each system had a separate clean air (CA; purified compressed laboratory air) exposure sector serving as controls (6 positions per ALI exposure system). Incubator control cell cultures were important to assess the impact of the ALI exposure system itself on the cultured cells. The temperature of each module containing the cells was continuously measured and controlled via external water baths, and although the cabinet was heated to 39.4°C, the modules themselves had to be cooled down to 37°C for optimal cell culture environment. Humidified aerosol and CA (85% RH) were operated with a 100-mL/min flow rate over every position in the ALI exposure system, as described by Mülhopt et al. (2016). Every evening the ALI exposure systems were dried using filtered ambient air, and the tubing to and from the modules was also dried by starting a filtered ambient air exposure ($\sim$30% RH) with an increased flow rate of 200 mL/min for 20 min. Between different aerosol exposures, the reactors were taken apart and cleaned with 70% ethanol. The impactors were cleaned once a week, as well as before changing the aerosol.

Estimation of the particle deposition in ALI. The deposited PM mass per area was calculated using the following equation.

$$Deposited\ mass\ per\ area\ \left[ng/cm^2\right] = \frac{\eta \times Q \times N \times t \times \rho_p \times V_p}{A},$$

where η is the deposition efficiency; Q is the aerosol flow; N is the particle number concentration (particle count per volume); t is the duration of the exposure; ρ_p is the particle density; V_p is the particle volume, assuming spherical particles; and A is the area of the deposition plate. The size-dependent deposition efficiency of particles (η) in the ALI exposure system is calculated using the theory described by Lucci et al. (2018). In the model, the deposition of particles is generally controlled by size-dependent diffusion and sedimentation mechanisms. Large particles deposit by sedimentation, whereas small particles deposit by diffusion. The particle deposition efficiency is controlled by various parameters (e.g., particle size and density, aerosol flow, temperature, pressure, and geometry of the system). In the present study, the size-dependent particle number concentration was used, which was measured by the SMPS at line D. The mean effective density of each aerosol type was calculated by forcing the mass concentration measured by SMPS to be equal to the mass concentration measured by a TEOM. Particle density influences the calculations in two ways: first, determining the deposition efficiency, and second, and more importantly, by converting the deposited number of particles to deposited mass. Aerosol flow and temperature were 100 mL/min and 37°C, respectively.

Cell lines and ALI exposure. A549 human alveolar epithelial cells (ATCC; CCL-185) and EA.hy926 hybrid human endothelial cells (kindly provided by Dr. S. Moertl, HelmholtzZentrum) were routinely cultured in high-glucose Gibco Dulbecco's Modified Eagle Medium: Nutrient Mixture F-12 (DMEM/F-12) (ThermoFisher Scientific; 31331-028) supplemented with 5% (vol/vol) fetal bovine serum (FBS) (ThermoFisher Scientific; 10500-064), and 100 U/mL penicillin and 100 μg/mL streptomycin (P/S; Sigma-Aldrich; P4333) in a humidified incubator at 37°C and 5% carbon dioxide (CO_2). For the mono- and coculture exposure experiments, A549 cells were seeded on the same day on transferrable 24-mm Transwell inserts with a polyester membrane (0.4−μm pore-size; type #3450; Corning) 96 h before the exposure experiments at a density of 1.8×10^5cells/mL per insert (3.8×10^4cells/cm^2 growth area) with 1.5 mL of cell culture medium provided at the basal compartment of the Transwell. Forty-eight hours after the initial cell seeding, the culture medium on the apical side for both cell models was removed to generate ALI conditions, and fresh cell culture medium was added in the basal compartment. Twenty-four hours later, the inserts for the coculture were inverted; 1×10^5 EA.hy926 cells per insert (0.21×10^4cells/cm^2 growth area) were seeded in 750 μL of medium; and after 1 h, the insert was turned back and fresh medium was added to the basolateral compartment of the Transwell. For the monoculture, the medium was renewed to ensure equal treatment of both cell culture models. On Day 5, the day of the exposure experiments, inserts with mono- and cocultures were placed

in the exposure modules of the ALI exposure system (Vitrocell Automated Exposure Station Standard Version) with 1.8 mL serum-free DMEM/F12 medium supplemented with 1% P/S and 15 mM *N*-2-hydroxyethylpiperazine-*N*-2-ethane sulfonic acid (HEPES) buffer solution (ThermoFisher Scientific; 15630-056) at the basolateral compartment. Cells were then exposed for 4 h to the conditioned (85% RH, 37°C) and differently diluted aerosols [undiluted (1:1), 1:3, 1:10, and 1:30]. All experiments were performed in at least three independent exposures. After the exposure, the effects of the aerosols on the cells were examined with several assays, and the exposure medium was collected on ice for direct analyses or frozen at −80°C for later analyses.

Immunofluorescence

To check for a confluent cell monolayer, the membranes were cut out from the Transwell inserts on the day of the exposure and were washed twice in phosphate-buffered saline (PBS), fixed with 4% formaldehyde (Paraformaldehyde; Carl Roth; 4980.1) for 12 min, and washed three times in 0.1% bovine serum albumin (BSA) (Sigma-Aldrich; A8412) in PBS, before staining with Phalloidine A488 (1:100; Sigma-Aldrich; 49409) and 4′,6-diamidino-2-phenylindole (DAPI) (1:1,000; Sigma-Aldrich; D9542) in 1% BSA and 0.1% Triton-X in PBS for 1 h at RT. Membranes were washed three times in PBS, once in double-distilled water, and embedded in fluorescence mounting medium (Glycergel; DAKO; Agilent; C056330-2). Slides were observed on a Lionheart FX Automated Microscope and pictures captured for illustration.

Cell viability assay and live cell microscopy. To determine cell viability, immediately after the exposure, A549 inserts were transferred to a 6-well plate, washed once with PBS before adding 1 mL prewarmed fresh exposure medium (serum-free DMEM/F12+1% P/S and 15 mM HEPES) with 10% PrestoBlue HS Cell Viability Reagent (ThermoFisher Scientific; A13262) to the apical and basolateral compartments. After an incubation of 45 min at 37°C in the incubator, aliquots of the basal and apical medium were pipetted into a 96-well plate, and the quantification of metabolically active cells was performed by measuring the fluorescence at 570 nm with a spectrophotometer (MULTISKAN SKY Microplate Spectrophotometer; ThermoFisher Scientific). The results are presented as percentage cell viability compared with incubator control from at least four independent exposures and one technical replicate, respectively. After the PrestoBlue assay, inserts were washed twice with PBS before 600 µL of staining solution [Hoechst; 33342; 5 µg/mL (Sigma-Aldrich; B2261) and propidium iodide (PI), 25 µg/mL (Sigma-Aldrich; P41770) in serum-free cell culture medium (DMEM/F12+1 % P/S] was added for 45 min at 37°C. This was followed by two further PBS washing steps, the addition of prewarmed PBS below and above the insert, and the capturing of the image with a live cell microscope (Lionheart FX automated microscope) at 37°C.

Cell membrane damage assay. For assessing aerosol-induced membrane integrity as a measure of cytotoxicity, the release of lactate dehydrogenase (LDH) was immediately determined from the medium that had been directly collected after exposures by the Cytotoxicity Detection Kit^{Plus} (L-LDH; Roche; 11644793001) in a 96-well plate. Cell culture medium was used as the blank. The kit was used according to the manufacturer's recommendation with the addition of a LDH standard curve ranging from 4 to 250 mU/mL (L-LDH; Roche; 10127230001). After 10 min, the quantification of LDH release was performed by measuring the absorbance at 493 nm with a spectrophotometer (MULTISCAN SKY Microplate Spectrophotometer). The results are shown as LDH concentration in microunits per milliliter calculated with the help of standard curves from at least four independent exposures and, in each case, four (monoculture) or two (coculture) technical replicates.

Oxidative stress analysis. Malondialdehyde (MDA), an indicator of cellular oxidative stress, was measured from the frozen collected sample media using the liquid chromatographic (LC) MS/MS method (API 4000 Triple Quadrupole system, AB Sciex in positive MRM mode), as previously described by Wu et al. (2017b). Shortly afterward, frozen samples were thawed and 20 µL of cell culture medium was mixed with 25 µL of 100 ng/mL d_2-MDA and 500 µL of 0.5 mM 2,4-dinitrophenylhydrazine (DNPH; Sigma-Aldrich; D199303) in 1% formic acid solution. Derivatization was conducted at 37°C under 300 rpm for 70 min in a Thermomixer C (Eppendorf) before 700 µL of *n*-hexane (high-performance LC-grade; VWR) was added, shaken, and centrifuged at 9,390 × *g* for 5 min Heraeus Biofuge Pico Centrifuge (Thermo Scientific). The *n*-hexane supernatant was collected, and the extraction procedure was repeated once. Following this, the collected *n*-hexane supernatant was combined and dried by nitrogen in a Vapotherm Basis Mobil I (Barkey) at RT. The dried residue was redissolved in 50 µL of methanol:0.1% formic acid (80:20, vol/vol). After the liquid–liquid extraction, the MDA adduct was analyzed by LC-MS/MS (capillary voltage 4.5 kV, source temperature 350°C, column compartment set at 20°C) in multiple reaction, and the isocratic separation was conducted with a constant flow of 200 µL/min of mobile phase. Each sample was injected twice with 10 µL injection volume for each measurement. A standard calibration curve with standard concentrations of MDA ranging from 0.5 to 20 ng/mL was set up for quantification. Data are presented as MDA in nanograms per milliliter from at least three independent exposures with one technical replicate.

Comet assay. Immediately after the exposure, inserts were washed twice with PBS and cells were harvested with 0.5% Trypsin-ethylenediaaminetetraacetic acid (EDTA) (Sigma-Aldrich; T4174) for 3 min (for A549 cells) or 6 min (for EA.hy926 cells). Trypsin-EDTA was inhibited with FBS, and the cell types were collected separately. The cells were centrifuged at 0.2 × *g* and 4°C and then resuspended in 1 mL of cold PBS. Cells were counted with Trypan Blue in an automated cell counter (Luna-II; Logos Biosystems; BioCat). The alkaline version of the comet assay was performed according to the mini-gel comet assay method previously described (Di Bucchianico et al. 2017) to detect DNA single- and double-strand breaks, as well as alkaline labile sites. Cells exposed to 30 µM hydrogen peroxide for 5 min on ice were used as positive controls. On each slide, eight mini-gels were prepared, including untreated controls, exposed cells, and positive controls for both A549 and EA.hy926 cells. At least three independent slides per condition were prepared, and 100 nucleoids per mini-gel were scored using CometScore (version 2.0; TriTek Corp.) on 1:10.000-dilution SYBR Green (ThermoFisher Scientific; S7563) stained slides. A Lionheart FX automated microscope was used to take 20× magnification micrographs of the stained slides. Data are shown as percentage DNA breaks (% DNA in tail) from at least three independent exposures with two technical replicates.

IL-8 measurement. Aliquots of the collected and −80°C-stored exposure media were thawed and analyzed in a 96-well plate, using the enzyme-based immunosorbent assay (ELISA; R&D Systems; DY208) for the pro-inflammatory cytokine IL-8, according to manufacturer's instruction. In brief, a 96-well plate was coated with 100 µL of diluted human IL-8 capture antibody overnight at RT. On the next day, the plate was washed three times with wash buffer [0.05% Tween 20 (Santa Cruz; 9005-64-5) in PBS, pH 7.2–7.4], blocked with 300 µL block buffer (1% BSA, pH 7.2–7.4) for 1 h, after which the washing step was repeated. Thawed samples of the A549 monoculture were diluted 1:2 and samples of the coculture 1:3 in reagent diluent (0.1% BSA and 0.05% Tween 20 dissolved in PBS) and IL-8 standards were prepared (31–2,000 pg/mL). One hundred microliters of either the samples

or the standards were added to the plate for 2 h at RT. After washing three times with wash buffer, the plate was incubated with 100 µL of detection antibody for 2 h at RT. The washing step was repeated, and 100 µL of streptavidin–horseradish peroxidase was added to each well for 20 min. After another washing step, 100 µL of 3,3′,5,5′-tetramethylbenzidine (TMB; Cell Signaling Technologies; 7004P6) was used as an substrate and incubated for 20 min before 50 µL of stop solution (sulfuric acid) was added, and the fluorescence was measured at 450 and 540 nm in a microplate reader (Varioskan Lux multimode microplate reader). Results are presented as IL-8 in picograms per milliliter from at least four independent exposures with one technical replicate.

Angiogenesis Assay

EA.hy926 cells were seeded at a density of 100,000 cells per well (2.6×10^4cells/cm^2 growth area) in a 12-well plate. After 24 h, the attached cells were treated with a 1:1 mixture of fresh medium and conditioned medium (CM) for 24 h. The CM represents the exposure medium that was collected and stored at −80°C after the 4-h exposure to the different undiluted aerosols. After 24 h, the cells were trypsinized and seeded in fresh cell culture medium at 2×10^4 cells per well (6.2×10^4cells/cm^2 growth area) in a 96-well plate precoated with a growth factor-reduced BME Matrigel (Cultrex *in vitro* angiogenesis assay; R&D Systems; 3470-096-K). Tube formation was captured 24 h after seeding (10× objective; Lionheart FX Automated Microscope; BioTek). The angiogenic potential, which indicates the capacity of a compound to increase or decrease the formation of capillary-like structures, was calculated with the formula established by Aranda and Owen (2009).

$$Angiogenic\ score = \left(\frac{(No.\ of\ sprouting\ cells)\times 1 + (No.\ of\ connected\ cells)\times 2 + (No.\ of\ polygons)\times 3}{Total\ number\ of\ cells}\right) + (0, 1\ or\ 2)$$

The addition of 0, 1, or 2 to the total value depended on the presence of a complex mesh. No complex mesh is represented by the addition of 0 points; for the existence of luminal structures consisting of two to three cell layers, an addition of 1 point is necessary; and for luminal structures of greater than three cell layers, an additional value of 2 is added. Results are presented as Angiogenic score from at least three independent experiments and two technical replicates.

Statistical methods. Each experiment was performed at least in triplicate. The results of three or more independent experiments were expressed as the mean ± standard error of the mean (SEM). Differences between the groups were analyzed using one-way analysis of variance (ANOVA) with the Welch-Satterthwaite approximation for unequal variances (Welch 1947). Multiple comparisons using the Bonferroni correction to control the inflation of type I errors were conducted for all ANOVA results with a $p < 0.05$ as post hoc analysis for sample comparison. All data were analyzed with R environment (RStudioTeam 2019, http://www.rstudio.com/). Graphs were illustrated using GraphPad Prism for Windows (version 9.0.0; GraphPad Software).

Results

Characterization of the SOA Components of the Two Aerosol Types

All online instruments confirmed stable and reproducible aerosol feeds and aging conditions over the entire exposure period of 4 h (Figure S1A–E). Moreover, BC and OC concentrations were similar for both precursors. In addition, strong similarities between both precursors were observed for averages of geometric mean of particle size, equivalent photochemical ages, and OC fractions. An overview of the SOA concentrations and properties, as well as of the bare SPs, is compiled in Table 1. TEM micrographs of both SOAs revealed similar particle shapes of soot agglomerates coated with organic material, whereas pure SPs seemed to retain their more fractal structures (Figure S2). The particle number of SOA_{NAP}-SP was slightly higher compared with $SOA_{\beta PIN}$-SP (Table 1), and spontaneous nucleation of SOA_{NAP}-SP, forming particles with a mobility diameter of <50 nm, occurred to a minor extent (Figure S1F). Consequently, the estimation of the particle mass deposition suggested a 1.5-fold higher deposition of SOA_{NAP}-SP (28 ng/cm^2) compared with $SOA_{\beta PIN}$-SP (17 ng/cm^2).

To explore how $SOA_{\beta PIN}$-SP is chemically distinct from SOA_{NAP}-SP, we performed untargeted GC × GC-TOFMS analysis for the SVOCs. The chemical composition of the two generated SOAs differed widely in individual molecular composition, compound classes, and oxidation state (Figure 2A–F). In GC × GC with a nonpolar column in the first and a polar column in the second

Table 1. Physical and chemical properties of unaged pure soot particles (SP, CAST soot; 1 mg/m^3) or atmospheric photooxidation (aging) by OH radicals in a potential aerosol mass (PAM) reactor of SP (CAST soot; 1 mg/m^3) together with either naphthalene (4 mg/m^3) or β-pinene (4 mg/m^3), forming SOA_{NAP}-SP and $SOA_{\beta PIN}$-SP, respectively.

		SP		SOA_{NAP}-SP		$SOA_{\beta PIN}$-SP	
Categories	Instrument	Mean ± SD	*n*	Mean ± SD	*n*	Mean ± SD	*n*
BC (mg/m^3)	Aethalometer	1.3 ± 0.1	7	1.5 ± 0.1	10	1.4 ± 0.1	11
BrC content (%)	Aethalometer	12 ± 1	7	32 ± 1	10	22 ± 1	11
Days atmospheric OH age [d (*n*)][a]	PTR-MS	0	7	2.9 ± 0.4	10	2.8 ± 0.2	11
Particle number concentration (*n*/cm^3)	CPC	$1.3 \times 10^6 \pm 0.3 \times 10^6$	7	$1.4 \times 10^6 \pm 0.2 \times 10^6$	10	$0.9 \times 10^6 \pm 0.2 \times 10^6$	11
Particle geometric mean diameter (nm)	SMPS	117 ± 1	7	114 ± 1	10	117 ± 1	11
Total EC (mg/m^3)	Carbon analyzer	0.7 ± 0.1	5	1.0 ± 0.2	10	0.7 ± 0.1	11
Total OC (mg/m^3)	Carbon analyzer	0.3 ± 0.2	5	1.1 ± 0.2	10	1.0 ± 0.2	11
OC_1 (mg/m^3)	Carbon analyzer	0.01 ± 0.01	5	0.2 ± 0.05	10	0.1 ± 0.03	11
OC_2 (mg/m^3)	Carbon analyzer	0.03 ± 0.02	5	0.3 ± 0.05	10	0.3 ± 0.05	11
OC_3 (mg/m^3)	Carbon analyzer	0.2 ± 0.3	5	0.5 ± 0.1	10	0.5 ± 0.1	11
OC_4 (mg/m^3)	Carbon analyzer	0.06 ± 0.08	5	0.1 ± 0.05	10	0.1 ± 0.04	11
Deposition (ng/cm^2)	Calculation	9 ± 1	5	28 ± 2	10	17 ± 2	11
H_2O_2-equivalent (µmol/m^3)	OPROSI	0.02 ± 0.05	3	14.1 ± 0.9	2	3.6 ± 0.5	3
O/C (ratio)	AMS	—	0	0.77 ± 0.06	10	0.61 ± 0.02	11

Note: Results are presented as mean ± SD. This reflects the reproducibility of *n* indicated independent experiments. —, no data available; AMS, high-resolution time-of-flight aerosol mass spectrometer; BC, black carbon; BrC, brown carbon; CPC, condensation particle counter; EC, elemental carbon; H_2O_2, hydrogen peroxide; OC, organic carbon; OH, hydroxy; PTR-MS, quadrupole proton–transfer reaction mass spectrometer; OPROSI, online particle-bound reactive oxygen species instrument; SD, standard deviation; SMPS, scanning mobility particle sizer.

[a]Assuming an average ambient hydroxyl radical concentration of 10^6molecules/m^3.

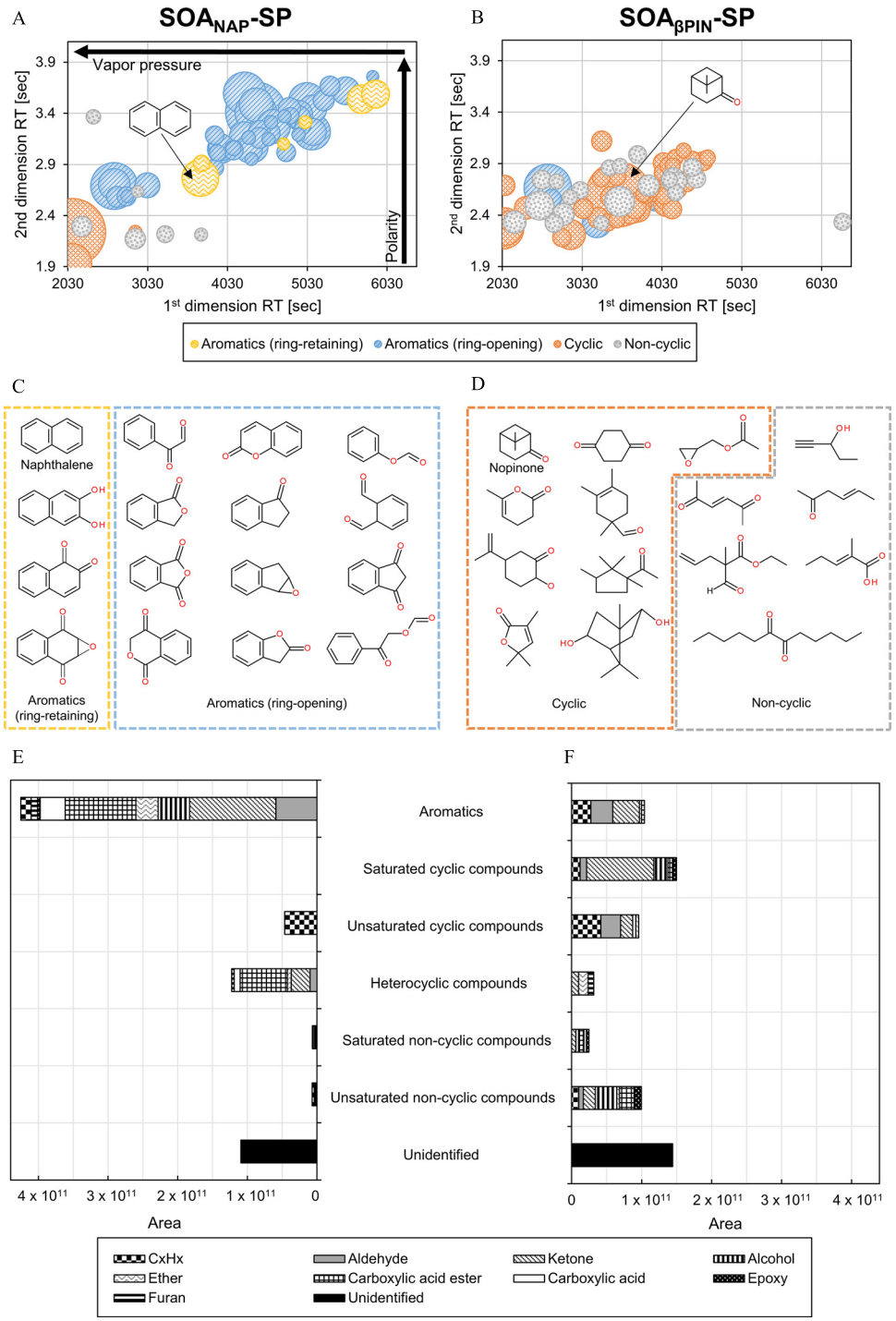

Figure 2. Chemical characterization of SOA_{NAP}-SP and $SOA_{βPIN}$-SP. (A,B) GC × GC-TOFMS bubble plots for SOA_{NAP}-SP (A) and $SOA_{βPIN}$-SP (B) at atmospheric OH age ≈ 3 d. Bubble sizes correspond to their respective peak areas. (C,D) Assignment of representative peaks from GC × GC-TOFMS for SOA_{NAP}-SP (C) and for $SOA_{βPIN}$-SP (D) to their molecular formulas via comparison with NIST mass spectral library and retention indices (excluding peaks with inconclusive MS spectra). (E,F) Areas of the 100 peaks with the highest signal intensities from GC × GC-TOFMS classified by compound classes and functional groups for SOA_{NAP}-SP (E) and for $SOA_{βPIN}$-SP (F). The classified 100 compounds account for 77.4% and 60.4% of the total abundance for SOA_{NAP}-SP and $SOA_{βPIN}$-SP, respectively. Corresponding numerical data for (A–D) are shown in Tables S1 and S2 and for (E,F) in Tables S3 and S4. Note: GC × GC-TOFMS, comprehensive two-dimensional gas chromatography–time-of-flight mass spectrometer; MS, mass spectrometer; NIST, National Institute of Standards and Technology; OH, hydroxyl; $SOA_{NAP\text{-}SP}/SOA_{βPIN}$-SP, soot particles (SP, CAST soot; 1 mg/m^3) together with either naphthalene (4 mg/m^3) or β-pinene (4 mg/m^3) photochemically aged with OH radicals in a potential aerosol mass reactor.

retention dimension, compounds were first separated according to their vapor pressures, corresponding to the respective carbon number and boiling point on the *x*-axis, and by polarity on the *y*-axis (Figure 2A,B). The compounds were classified into both ring-opening and -retaining aromatics, as well as cyclic and noncyclic compounds, based on their appearance in the 2D chromatogram and mass spectrometric signature (Figure S3). SOA_{NAP}-SP was clearly dominated by aromatic structures. Aromatic compounds, retaining the naphthalene carbon backbone of two six-rings, eluted slightly faster in the second dimension compared with the ring-

opening aromatic compounds and, therefore, were located below the ring-opening aromatics in the 2D chromatogram. For $SOA_{\beta PIN}$-SP, the region between 3,000 and 5,000 s revealed peaks of highest abundance, corresponding to a boiling point range of $\sim 170°C$ to 290°C for linear alkanes with a molecular weight of $\sim 140–230$ Da and carbon numbers between C_{10} and C_{16}. For SOA_{NAP}-SP, the region with peaks of highest abundance was between 3,700 and 6,000 s, corresponding to a boiling point range of $\sim 220°C$ to 330°C for linear alkanes with a molecular weight of $\sim 170–270$ Da and carbon numbers between C_{12} and C_{19}.

In all aging experiments, we detected more individual compounds for $SOA_{\beta PIN}$-SP than for SOA_{NAP}-SP within the assessable boiling point range. At a minimum peak S/N of 1,000 the total peak number for SOA_{NAP}-SP and $SOA_{\beta PIN}$-SP was 397 and 798 peaks, respectively. The top 100 peaks with the highest peak intensities presented in Figure 2A,B,E,F contributed to 77.4% and 60.4% of the total peak intensity for SOA_{NAP}-SP and $SOA_{\beta PIN}$-SP, respectively (Figure S4, Tables S1 and S2). Furthermore, SOA_{NAP}-SP consisted of fewer, but more abundant, compounds in signal intensity (Figure S4A). Despite performing an elaborated cleaning procedure, carryover effects between experiments could not be fully avoided. However, Figure S4 illustrates that the carryover was limited when considering the chemical profiles and abundances, showing that the investigated two SOA types resulted in entirely different chemical species with respect to the detected molecular structures. For $SOA_{\beta PIN}$-SP, these compounds were mostly comprised of oxygenated cyclic and acyclic compounds (Figure 2D,F), whereas in SOA_{NAP}-SP, we mostly found aromatic structures (Figure 2C,E). DIP-HR-TOFMS measurements were performed for the analysis of higher oxidized compounds, exceeding the application range of GC × GC-TOFMS. Complex patterns of nonaromatic ($H/C > 1$) oxidized fragments ($O/C > 0$) with up to four oxygen atoms were recognized, although oligomers could not be unambiguously identified (Figure 3E,F). The DIP-HR-TOFMS measurements showed a lower H/C-ratio for SOA_{NAP}-SP, pointing again to its more aromatic structure compared with $SOA_{\beta PIN}$-SP. The resulting O/C values from the AMS measurements indicated a slightly higher photochemical oxidation of SOA_{NAP}-SP compared with $SOA_{\beta PIN}$-SP (Figure 3B,D). In addition, $SOA_{\beta PIN}$-SP appeared well within the triangular space spanned by the relative fractions of *m/z* 43 vs. *m/z* 44 (Figure S5).

Cytotoxic Effects after Exposure to Soot Aerosol Coated with SOAs

For our study we established two different cell culture models, one using an alveolar epithelial lung (A549) cell line as an ALI monoculture model and another using an A549/human endothelial (EA.hy926) cell line ALI coculture model (Figure 4A, graphical illustration). Immunofluorescence staining confirmed a confluent single cell layer in both cell culture models shortly before the aerosol exposure (Figure 4A, right panel). To explore how $SOA_{\beta PIN}$-SP and SOA_{NAP}-SP affect the cell culture models, we first performed a resazurin-based viability test on the A549 monoculture. Exposure to the undiluted pure SPs did not significantly decrease cell viability (Table S6). In addition, $SOA_{\beta PIN}$-SP did not significantly affect cell viability in all tested dilutions ($p > 0.05$) and exhibited slightly

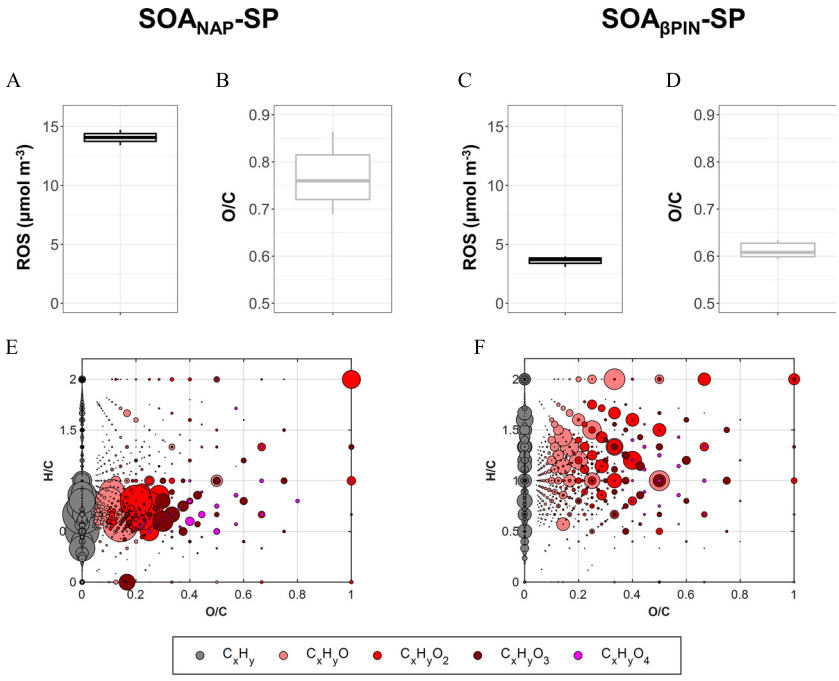

Figure 3. Oxidation state of SOA_{NAP}-SP and $SOA_{\beta PIN}$-SP. (A,C) Occurrence of reactive oxygen species (ROS) in SOA_{NAP}-SP (A) and $SOA_{\beta PIN}$-SP (C) by measuring H_2O_2 with an online particle-bound ROS instrument (OPROSI) in micromoles per meter cubed of n independent experiments (SOA_{NAP}-SP: $n = 2$, $SOA_{\beta PIN}$-SP: $n = 3$). (B,D) O/C ratios determined by AMS for SOA_{NAP}-SP (B) and $SOA_{\beta PIN}$-SP (D) of n independent experiments (SOA_{NAP}-SP: $n = 10$, $SOA_{\beta PIN}$-SP: $n = 11$). (A–D) The upper and lower hinges of the box plots represent the first and third quartiles (the 25th and 75th percentiles) of the distribution. The midline in the box is the median and the whiskers extend from the highest, respectively lowest, value that is within 1.5 × IQR of the hinge, where IQR is the distance between the first and third quartile. (E,F) Van-Krevelen Plots for DIP-HRTOFMS measurements (average of 4 independent experiments, respectively) of SOA_{NAP}-SP (E) and $SOA_{\beta PIN}$-SP (F). The size of the depicted circles represents the relative abundance of ions in the mass spectrum. Other than for the AMS, the mass fragments at *m/z* 43.9898 of CO_2^+ and *m/z* 27.9949 of CO^+ are not considered for the DIP results. Corresponding numerical data for (A–D) are shown in Table 1, and (E,F) in Excel Tables S7 and S8. Note: AMS, high-resolution time-of-flight aerosol mass spectrometer; CO_2, carbon dioxide; DIP-HRTOFMS, direct insertion probe high-resolution time-of-flight mass spectrometer; IQR, interquartile range; OH, hydroxyl;$SOA_{NAP\text{-}SP}/SOA_{\beta PIN}$-SP, soot particles (SP, CAST soot; 1 mg/m^3) together with either naphthalene (4 mg/m^3) or β-pinene (4 mg/m^3) photochemically aged with OH radicals in a potential aerosol mass reactor.

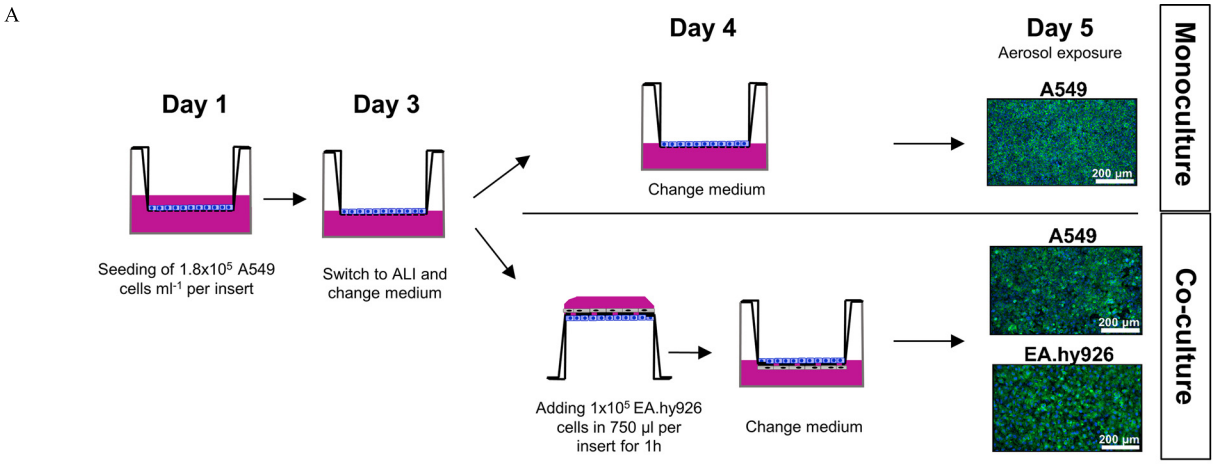

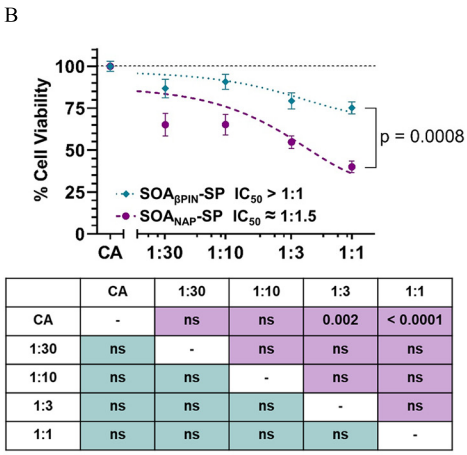

	CA	1:30	1:10	1:3	1:1
CA	-	ns	ns	0.002	< 0.0001
1:30	ns	-	ns	ns	ns
1:10	ns	ns	-	ns	ns
1:3	ns	ns	ns	-	ns
1:1	ns	ns	ns	ns	-

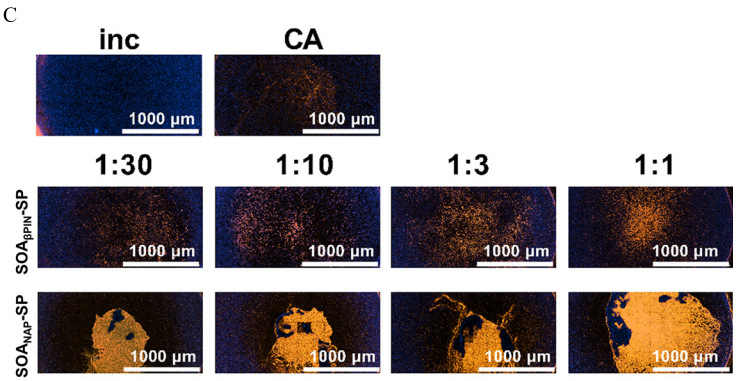

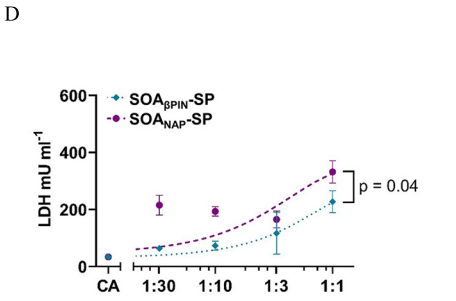

	CA	1:30	1:10	1:3	1:1
CA	-	0.0007	0.002	0.01	<0.0001
1:30	ns	-	ns	ns	0.048
1:10	ns	ns	-	ns	0.02
1:3	ns	ns	ns	-	0.003
1:1	0.02	ns	ns	ns	-

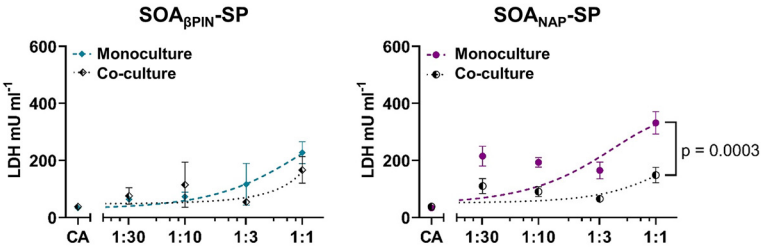

	1:30	1:10	1:3	1:1
CA	ns	ns	ns	ns
1:30		ns	ns	ns
1:10			ns	ns
1:3				ns

	1:30	1:10	1:3	1:1
CA	0.02	ns	ns	<0.00001
1:30		ns	ns	ns
1:10			ns	ns
1:3				0.01

Figure 4. Cell viability and LDH release after 4-h exposure to SOA$_{NAP}$-SP and SOA$_{βPIN}$-SP. (A) Schematic overview of the cell seeding procedure of mono- and coculture, as well as representative immunofluorescences images of mono- (A549; upper image) and coculture (A549/EA.hy926; lower image) on the day of aerosol exposure, stained for actin filaments (phalloidin, green) and nuclear stain (DAPI, blue). Scale bar: 200 µm. (B) Cell viability of A549 monoculture after the exposure to SOA$_{βPIN}$-SP and SOA$_{NAP}$-SP measured by resazurin-based assay. Results are presented as the mean cell viability compared with the incubator ctrl ± SEM of n independent experiments (SOA$_{βPIN}$-SP: $n = 4$, SOA$_{NAP}$-SP: $n = 5$ for all dilutions and CA ctrl: $n = 8$) and dotted lines denote the regression line for the respective SOA forced through the CA ctrl. (C) Propidium iodide staining (PI, red) of A549 monoculture after 4 h exposure with SOA$_{βPIN}$-SP and SOA$_{NAP}$-SP for all dilutions, as well as a CA ctrl. Hoechst nuclear stain (blue). Scale bar: 1,000 µm. Shown are representative images of at least three independent experiments. (D) LDH release (mU/mL) of A549 monoculture after the exposure to SOA$_{βPIN}$-SP and SOA$_{NAP}$-SP. (E) Comparison of LDH release (mU/mL) of the mono- and coculture after the exposure to SOA$_{βPIN}$-SP (left panel) and SOA$_{NAP}$-SP (right panel). (D,E) Results are presented as absolute values ± SEM of n independent experiments (SOA$_{βPIN}$-SP: $n = 4$, SOA$_{NAP}$-SP: $n = 5$ for all dilutions, and CA ctrl: $n = 9$) and dotted lines denote the regression line for the respective cell culture models and SOA forced through the CA ctrl. (B,D,E) Aerosol exposure groups were compared by performing a one-way ANOVA and statistical significance was calculated with multiple comparisons for the dilutions within one aerosol exposure group using the Bonferroni correction. p-Values are presented in the graph and in the tables below the graphs. Corresponding numerical data for (B,D,E) are shown in Tables S6 and S7. Note: ANOVA, analysis of variance; CA, clean air; ctrl, control; DAPI, 4′,6-diamidino-2-phenylindole; inc, incubator; LDH, lactate dehydrogenase; OH, hydroxyl; SEM, standard error of the mean; SOA, secondary organic aerosol; SOA$_{NAP\text{-}SP}$/SOA$_{βPIN}$-SP, soot particles (SP, CAST soot; 1 mg/m^3) together with either naphthalene (4 mg/m^3) or β-pinene (4 mg/m^3) photochemically aged with OH radicals in a potential aerosol mass reactor.

lower viability (78%) following undiluted aerosol exposures [half-maximal inhibitory concentration (IC_{50}) > 1:1 dilution; Figure 4B]. In contrast, cells exposed to SOA_{NAP}-SP had lower cell viability in the range from 70% cell viability for the 1:30 diluted aerosol to the significant ($p < 0.0001$) 40% for the undiluted aerosol ($IC_{50} = 1{:}1.5$; Figure 4B) compared with control cells. The undiluted SOA_{NAP}-SP aerosol cell exposures showed significantly lower viability than undiluted $SOA_{\beta PIN}$-SP treatments ($p = 0.0008$). This significant difference was also confirmed by normalizing to the deposition that is needed to achieve the respective IC_{50} values of $SOA_{\beta PIN}$-SP and SOA_{NAP}-SP. By liner regression analysis, the normalized mass deposition for SOA_{NAP}-SP ($R^2 = 0.6$, $p = 0.0005$) resulted in an IC_{50} value of 18 ng/cm^2, whereas the IC_{50} value for $SOA_{\beta PIN}$-SP ($SOA_{\beta PIN}$-SP: $R^2 = 0.7$, $p = 0.001$) did not even reach its highest concentration. No linear regression could be calculated for the exposure with SP ($R^2 = 0.01$) because of the similar results in all dilutions. No significant difference in cell viability was observed for the CA controls compared with the incubator controls (100% cell viability). The resazurin-based assay was not conducted with the coculture model owing to space limitations in the ALI exposure system. The results from the cell viability assay of the monoculture were also corroborated by live cell microscopy, where we saw a higher number of dead cells after the exposure to SOA_{NAP}-SP than to $SOA_{\beta PIN}$-SP and only a slightly higher number of dead cells in the CA control compared with the incubator controls (Figure 4C).

The difference in cell viability prompted a further elucidation of how the tested biogenic and combustion-derived SOAs affected the used cell cultures. In the monoculture, a concentration-dependent ($R^2 = 0.5$, $p = 0.03$) difference in LDH level (higher in exposed cells vs. control) was detected following exposure with $SOA_{\beta PIN}$-SP, with the highest effect at dilution 1:1 (undiluted). Compared with $SOA_{\beta PIN}$-SP, the exposure to SOA_{NAP}-SP in the monoculture led to the release of higher LDH concentrations in all dilutions with ~200 mU/mL in dilutions 1:30, 1:10, and 1:3 and 330 mU/mL in dilution 1:1 (undiluted) (Figure 4D). These aerosol-specific effects on LDH release in the monoculture were confirmed by the results observed with the coculture system, in which we monitored the same trends with a lower magnitude, but with no statistically significant effect compared with the monoculture (Figure 4E). Model systems exposed to CA were not significantly different from each other in LDH release (33 mU/mL for monoculture; 38 mU/mL for coculture).

Effects on Oxidative Stress and Genotoxicity by Soot Aerosol Coated with SOAs

Next, we investigated why SOA_{NAP}-SP induced a higher cytotoxic effect compared with $SOA_{\beta PIN}$-SP. No organic or inorganic peroxides were present in the undiluted pure soot aerosol (Table 1), 3.6 μmol/m^3 hydrogen peroxide (H_2O_2)-equivalent in the undiluted $SOA_{\beta PIN}$-SP and 14.1 μmol/m^3 H_2O_2-equivalent in the undiluted SOA_{NAP}-SP, indicating a higher oxidative potential of SOA_{NAP}-SP with respect to $SOA_{\beta PIN}$-SP (Figure 3A,C). These results were corroborated through analysis of MDA, a marker for cellular oxidative stress. Both in the mono- (Figure 5A) and the coculture (Figure 5B), exposure to SOA_{NAP}-SP induced the highest release of MDA in all dilutions (concentration-dependent; $R^2 = 0.98$, $p = 0.0002$) with a peak at the undiluted (1:1) aerosol (45 ng/mL). The exposure with $SOA_{\beta PIN}$-SP resulted in a concentration-dependent ($R^2 = 0.8$, $p = 0.15$) higher release of MDA, with the greatest release of 23.3 ng/mL (monoculture) and 18 ng/mL (coculture) at dilution 1:1 (undiluted) (Figure 5A,B). Also here, the cells exposed to undiluted pure soot had only a slightly higher release of MDA in the monoculture (12 ng/mL; SP column in Table S6) and in the coculture (11 ng/mL; SP column in Table S7). These findings of elevated oxidative stress markers after SOA exposure motivated the genotoxicity investigation, given that oxidative stress can cause DNA damage. Interestingly, the exposure with $SOA_{\beta PIN}$-SP and SOA_{NAP}-SP resulted in a flatter response compared with the MDA results for the dilutions from 1:10 until 1:1 (undiluted) for $SOA_{\beta PIN}$-SP (9–11% DNA breaks) and from 1:30 until 1:1 (undiluted) for SOA_{NAP}-SP (13–16% DNA breaks) in A549 cells in both cell culture models (Figure 5C,D). Remarkably, after the exposure to SOA_{NAP}-SP, we detected a significantly higher percentage of DNA breaks in EA.hy926 cells that were not directly exposed to the aerosols [7% DNA breaks (1:3), $p = 0.02$ to 1:10 dilution; 8% DNA breaks (1:10), $p = 0.03$ to 1:10 dilution], suggesting possible secondary genotoxic effects. Because of space limitations in the ALI exposure system, the baseline of DNA breaks were defined from the incubator control, showing 4% of DNA breaks. Moreover, the exposure to undiluted SP resulted in 8% DNA breaks of A549 cells in both cell culture models and 4% for EA.hy926 cells (SP column in Tables S6 and S7).

Impacts on Inflammatory Response and Angiogenesis by Soot Aerosols Coated with SOAs

The exposure to $SOA_{\beta PIN}$-SP resulted in a non–concentration-dependent response with IL-8 concentrations between 335 pg/mL and 382 pg/mL in the monoculture. SOA_{NAP}-SP, however, induced a higher concentration-dependent ($R^2 = 0.92$, $p = 0.002$) IL-8 release with 600 pg/mL at the undiluted (1:1) aerosol (Figure 6A). The CA control was at 341 pg/mL and the exposure to undiluted SP showed no further difference in IL-8 release (360 pg/mL; SP column in Table S6). Contrary to the results regarding cytotoxicity and oxidative stress, SOA exposures of the coculture resulted in a significantly higher IL-8 release compared with the monoculture in both aerosols and all dilutions (Figure 6B). Exposure of the coculture to SP had no significant effect on IL-8 release (520 pg/mL; SP column in Table S7). Moreover, we wanted to elucidate how the greater secretion of inflammatory cytokines may directly regulate the functional crosstalk between A549 and EA.hy926 endothelial cells. By treating EA.hy926 cells with conditioned media from the A549 exposure to the different aerosols, we found that only media from the SOA_{NAP}-SP exposure induced a higher angiogenic potential of EA.hy926 (Figure 6C,D). We saw the same effect with the conditioned medium from the coculture exposed to SOA_{NAP}-SP, where we found a significant difference compared with the CA control and even $SOA_{\beta PIN}$-SP (Figure 6C,D). No angiogenic effect of the conditioned media collected after the exposure to SP from both cell culture models was observed (Tables S6 and S7).

Discussion

The present study provides new insights into the impact of SOA of anthropogenic and biogenic volatile organic precursors in the presence of soot core particles in airway ALI model systems at the cellular and molecular levels. It was observed that the formation of an SOA layer by adsorption and condensation on freshly emitted SP could cause a substantial aggravation of toxic effects, differing from combustion-only SP, which caused only slight toxic effects. Thus, it could be expected that the toxicity of primary particulate emissions in the ambient air during a medium strong atmospheric aging (e.g., equivalent to a range of a few days) was enhanced. Here, SOAs formed from a biogenic (β-pinene) or a combustion-related organic precursor component (naphthalene) were investigated and compared. We showed that an in-depth physicochemical aerosol characterization delivered relevant information for inhalation toxicology studies and that the different chemical identity of tested aerosols may explain the different toxicological outcomes. Cells exposed to SOA_{NAP}-SP—here as surrogate for atmospherically processed

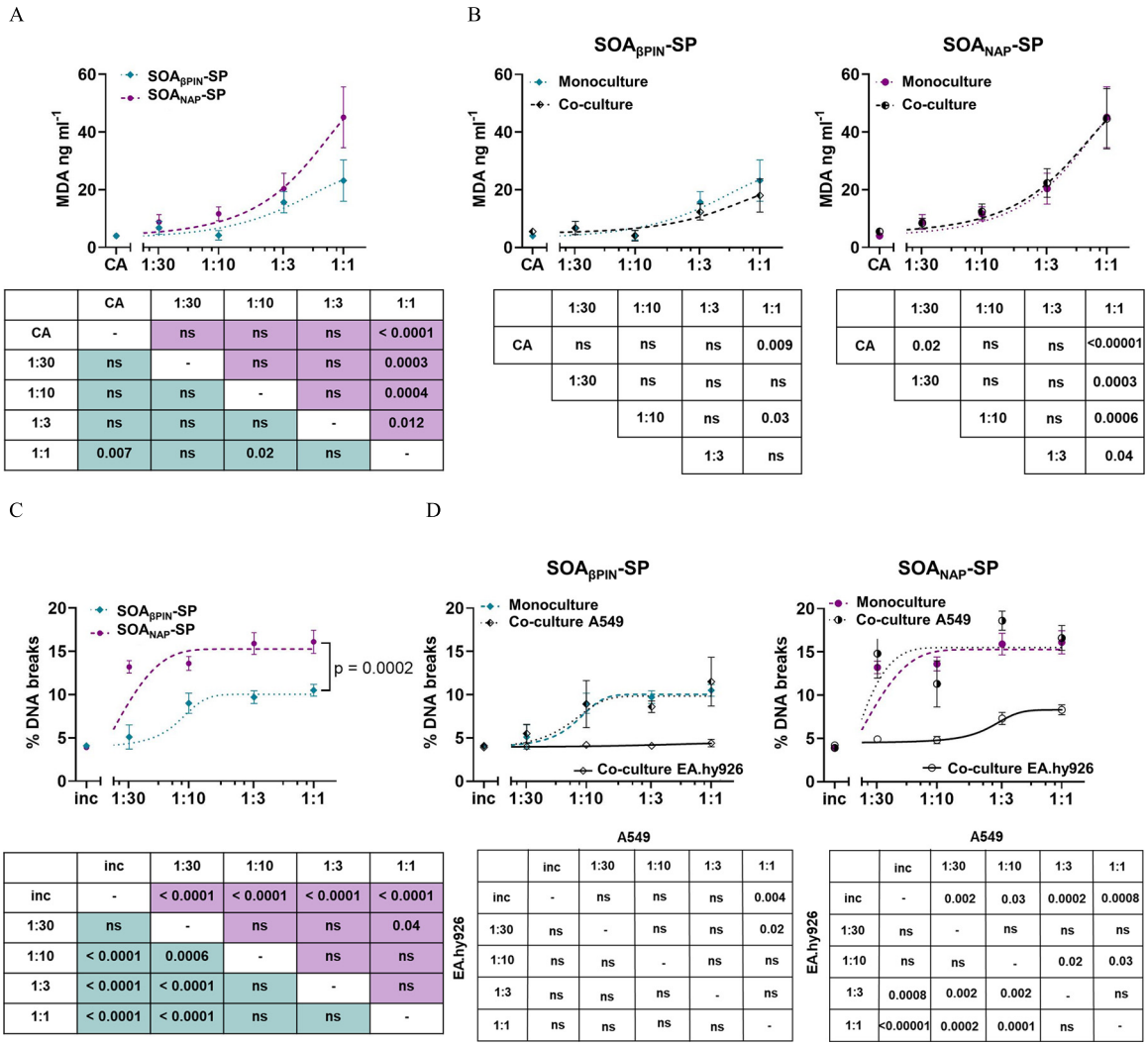

	CA	1:30	1:10	1:3	1:1
CA	-	ns	ns	ns	< 0.0001
1:30	ns	-	ns	ns	0.0003
1:10	ns	ns	-	ns	0.0004
1:3	ns	ns	ns	-	0.012
1:1	0.007	ns	0.02	ns	-

	1:30	1:10	1:3	1:1
CA	ns	ns	ns	0.009
1:30		ns	ns	ns
1:10			ns	0.03
1:3				ns

	1:30	1:10	1:3	1:1
CA	0.02	ns	ns	<0.00001
1:30		ns	ns	0.0003
1:10			ns	0.0006
1:3				0.04

	inc	1:30	1:10	1:3	1:1
inc	-	< 0.0001	< 0.0001	< 0.0001	< 0.0001
1:30	ns	-	ns	ns	0.04
1:10	< 0.0001	0.0006	-	ns	ns
1:3	< 0.0001	< 0.0001	ns	-	ns
1:1	< 0.0001	< 0.0001	ns	ns	-

A549 — EA.hy926

	inc	1:30	1:10	1:3	1:1
inc	-	ns	ns	ns	0.004
1:30	ns	-	ns	ns	0.02
1:10	ns	ns	-	ns	ns
1:3	ns	ns	ns	-	ns
1:1	ns	ns	ns	ns	-

A549 — EA.hy926

	inc	1:30	1:10	1:3	1:1
inc	-	0.002	0.03	0.0002	0.0008
1:30	ns	-	ns	ns	ns
1:10	ns	ns	-	0.02	0.03
1:3	0.0008	0.002	0.002	-	ns
1:1	<0.00001	0.0002	0.0001	ns	-

Figure 5. Induced oxidative stress and genotoxicity after 4-h exposure to SOA_{NAP}-SP and $SOA_{\beta PIN}$-SP. (A) MDA release (ng/mL) of A549 monoculture after the exposure to $SOA_{\beta PIN}$-SP and SOA_{NAP}-SP. (B) Comparison of MDA release (ng/mL) of the mono- and coculture after the exposure to $SOA_{\beta PIN}$-SP (left panel) and SOA_{NAP}-SP (right panel). Results are presented as absolute values ± SEM of n independent experiments ($SOA_{\beta PIN}$-SP: $n = 3$, SOA_{NAP}-SP: $n = 4$ for all dilutions, and CA ctrl: $n = 7$) and dotted lines denote the regression line for the respective cell culture models and SOA forced through the CA ctrl (A,B). (C) DNA breaks (in %) of A549 monoculture after the exposure to $SOA_{\beta PIN}$-SP and SOA_{NAP}-SP. (D) Comparison of DNA breaks (in %) of the mono- and co-culture (Coculture A549; Coculture EA.hy926) after the exposure to $SOA_{\beta PIN}$-SP (left panel) and SOA_{NAP}-SP (right panel). Results are presented as absolute values ± SEM of n independent experiments ($SOA_{\beta PIN}$-SP: $n = 4$, SOA_{NAP}-SP: $n = 5$ for all dilutions and inc ctrl: $n = 3$) and dotted lines denote the regression line for the respective cell culture models and SOA forced through the CA ctrl (C and D). (A–D) Aerosol exposure groups were compared by performing a one-way ANOVA and statistical significance was calculated with multiple comparisons for the dilutions within one aerosol exposure group using the Bonferroni correction. p-Values are presented in the graph and in the tables below the graphs. Corresponding numerical data for (A–D) are shown in Tables S6 and S7. Note: ANOVA, analysis of variance; CA, clean air; ctrl, control; inc, incubator; MDA, malondialdehyde; SEM, standard error of the mean; SOA, secondary organic aerosol; $SOA_{NAP\text{-}SP}/SOA_{\beta PIN}$-SP, soot particles (SP, CAST soot; 1 mg/m^3) together with either naphthalene (4 mg/m^3) or β-pinene (4 mg/m^3) photochemically aged with OH radicals in a potential aerosol mass reactor.

combustion emissions—exhibited lower cell viability, higher oxidative stress, and genotoxicity and induced inflammatory and angiogenic responses compared with those exposed to $SOA_{\beta PIN}$-SP. In addition, concentration-dependent biological effects were observed following exposures to $SOA_{\beta PIN}$-SP and SOA_{NAP}-SP in several assays. Moreover, the different toxicological responses in the used mono- and coculture systems pointed out the importance of using multicellular *in vitro* models to improve the understanding of possible cellular crosstalk.

Chemical Distinct Characteristics of SOAs Responsible for Cellular Effects

Chemical and physical transformation of VOCs in the atmosphere lead to the formation of amorphous solid or semi-solid SOA particles (Dennis-Smither et al. 2014); however, investigations of the *in vitro* toxicity of primary combustion emissions (i.e., of SPs) photochemically aged in the presence of SOAs are scarce. The photochemical aging of both naphthalene and β-pinene in the presence of soot aerosols resulted in SPs coated with SOA materials that simulated aged atmospheric SPs. These aerosols had similar physicochemical characteristics in terms of mass, size distribution, particle number, particle geometric mean diameter, and atmospheric OH radical age, as well as EC and OC content. This is of great importance because it remains unclear whether SOAs with similar physical characteristics also cause similar biological effects (Burkholder et al. 2017; Künzi et al. 2015; National Academies of Sciences, Engineering, and Medicine 2016). The present study shows that SOA_{NAP}-SP compared with $SOA_{\beta PIN}$-SP had an adverse outcome on cell viability, oxidative stress, genotoxicity,

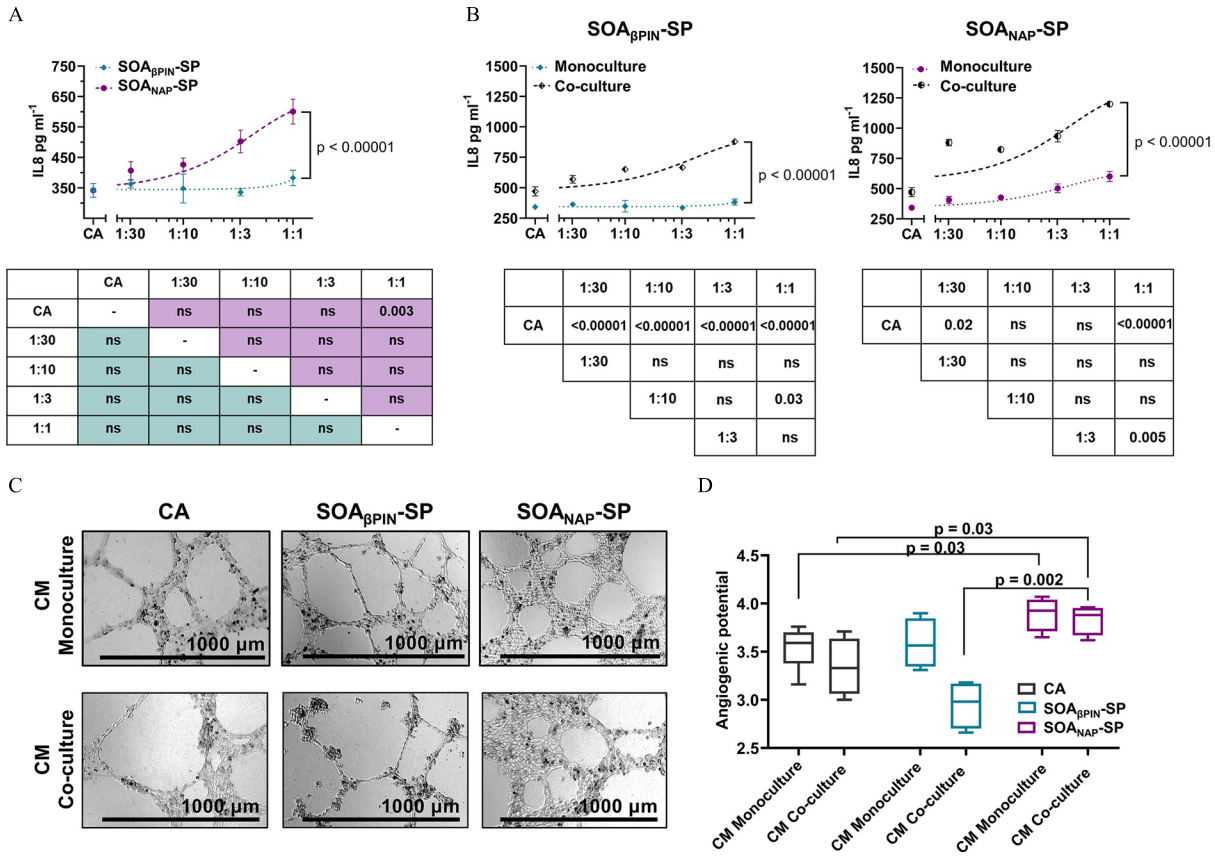

	CA	1:30	1:10	1:3	1:1
CA	-	ns	ns	ns	0.003
1:30	ns	-	ns	ns	ns
1:10	ns	ns	-	ns	ns
1:3	ns	ns	ns	-	ns
1:1	ns	ns	ns	ns	-

	1:30	1:10	1:3	1:1
CA	<0.00001	<0.00001	<0.00001	<0.00001
1:30		ns	ns	ns
1:10			ns	0.03
1:3				ns

	1:30	1:10	1:3	1:1
CA	0.02	ns	ns	<0.00001
1:30		ns	ns	ns
1:10			ns	ns
1:3				0.005

Figure 6. Inflammatory and angiogenic response triggered by SOA$_{NAP}$-SP and SOA$_{\beta PIN}$-SP. (A) IL-8 release (pg/mL) in A549 monoculture after the exposure to SOA$_{\beta PIN}$-SP and SOA$_{NAP}$-SP. (B) Comparison of IL-8 release (pg/mL) of the mono- and coculture after the exposure to SOA$_{\beta PIN}$-SP (left panel) and SOA$_{NAP}$-SP (right panel). (A,B) Results are presented as absolute values ± SEM of n independent experiments (SOA$_{\beta PIN}$-SP: $n = 4$, SOA$_{NAP}$-SP: $n = 5$ for all dilutions and CA ctrl: $n = 12$) and dotted lines denote the regression line for the respective cell culture models and SOA forced through the CA ctrl. Aerosol exposure groups were compared by performing a one-way ANOVA and statistical significance was calculated with multiple comparisons for the dilutions within one aerosol exposure group using the Bonferroni correction. p-Values are presented in the graph and in the tables below the graphs. (C,D) EA.hy926 cells were cultured for 24 h in media collected after the exposure to SOA$_{\beta PIN}$-SP and SOA$_{NAP}$-SP, as well as, CA control and then allowed to from tube structures on Matrigel for 24 h. Shown are representative images of EA.hy926 tubes from the indicated treatments (C) and quantification (D) of three independent experiments. Scale bar: 1,000 µm. Corresponding numerical data for (A–D) are shown in Tables S6 and S7. Note: ANOVA, analysis of variance; CA, clean air; CM, conditioned medium; ctrl, control; IL-8, interleukin-8; OH, hydroxyl; SEM, standard error of the mean; SOA, secondary organic aerosol; SOA$_{NAP\text{-}SP}$/SOA$_{\beta PIN}$-SP, soot particles (SP, CAST soot; 1 mg/m^3) together with either naphthalene (4 mg/m^3) or β-pinene (4 mg/m^3) photochemically aged with OH radicals in a potential aerosol mass reactor.

and inflammation consistent with previous studies (Chowdhury et al. 2018, 2019; Han et al. 2020) and, in addition, induced a pro-angiogenic potential in endothelial cells. This also holds true if we account for the calculated mass-specific cellular deposition, which was greater for SOA$_{NAP}$-SP. Even though this study confirmed the health risks of specific SOA compounds and pointed out the benefits of *in vitro* exposures in an ALI exposure system, it has its limitations. The applicability of ALI exposures to human exposures remains uncertain as long as it is difficult to determine respiratory tract deposition of airborne nanoparticles (Löndahl et al. 2014). However, calculations by Paur et al. (2011) for *in vitro* nanotoxicity studies suggested using ranges between 0.75 ng/cm^2 for realistic ambient exposure and 130 ng/cm^2 for worst-case occupational exposure representing daily dose levels. In the present study, the deposition ranged from 0.9 ng/cm^2 (1:30 dilution) to 28 ng/cm^2 (undiluted) for SOA$_{NAP}$-SP and from 0.6 ng/cm^2 (1:30 dilution) to 17 ng/cm^2 (undiluted) for SOA$_{\beta PIN}$-SP, covering realistic ambient exposure to mild occupational exposure conditions. Moreover, in a recent study, we showed that for aerosols with a comparable particle size distribution the difference between the deposition in lung tissue and ALI exposure system was less than a factor of 2 (Karg et al. 2020).

The chemical characterization revealed distinct qualitative differences in the chemical composition of SOA$_{\beta PIN}$-SP and SOA$_{NAP}$-SP, which is potentially responsible for the observed differences in the cellular toxicity. Thereby, the chemical composition of the derived SOA depended very much on the chemical functionality of the precursor and the low organic content of the SP seed. The detected chemical structures corresponded to typical first-generation degradation products of the respective precursor. For SOA$_{\beta PIN}$-SP, the major first-generation degradation product was nopinone in the particulate and acetone in the gas phase (Hohaus et al. 2015; Kaminski et al. 2017). In SOA$_{NAP}$-SP, we mostly found aromatic structures, which are well-known aging products originating from ring-opening and -retaining reactions of the aromatic precursors (Chan 2009). The photochemical degradation of naphthalene started with the addition of a OH radical, forming a hydroxyhexadienyl-type radical. From an intramolecular rearrangement, the first-generation product naphthol was formed. If the hydroxyhexadienyl-type radical reacts with oxygen, ring-opening structures may be formed, such as 2-formylcinnamaldehyde (Keyte et al. 2013). 1-Naphthol and 2-naphthol, which were generated in significant yields, may be further oxidized by other oxidants, such as hydroperoxides, and oxygen

to naphthoquinones (Keyte et al. 2013). Upon further oxidation, early generation products increase in oxygen-containing moieties and could polymerize under the applied conditions (Kenseth et al. 2018; Sato et al. 2016).

Moreover, differences in volatility of the formed compounds from β-pinene and naphthalene aging could be derived from the GC × GC signatures, generally indicating more volatile compounds for $SOA_{\beta PIN}$-SP. In SOA_{NAP}-SP, the aromatic structure was usually maintained and dominated the SOA composition, for which toxic effects on human health are well documented and include carcinogenic and mutagenic effects, as well as reproductive defects (Drwal et al. 2019; Gaspari et al. 2003; Perera et al. 2002).

Concerning elemental aerosol particle composition, the O/C value for SOA_{NAP}-SP (0.77) exceeded that of $SOA_{\beta PIN}$-SP (0.61), agreeing with a previous study about the photooxidation of naphthalene and α-pinene (Chowdhury 2018). In addition, the average carbon oxidation state (OS_C), which is calculated as $2 \times O/C – H/C$ was higher for SOA_{NAP}-SP (0.5) than for $SOA_{\beta PIN}$-SP (–0.43). SOA_{NAP}-SP, with 0.3 to 0.7, showed a similar range of OS_C as reported in the literature for emissions from residential logwood combustion (Hartikainen et al. 2020) and gasoline direct injection vehicles (Pieber et al. 2018) of the same photochemical age (~ 3 equivalent days). The OS_C increases upon oxidation owing to the formation of carbon–oxygen bonds and/or the breaking of carbon–hydrogen bonds through, for example, functionalization or fragmentation reactions (Kroll et al. 2011). In this context, the oxidative addition of polar functional groups to the carbon backbone could be observed for both aerosol types.

We found that $SOA_{\beta PIN}$-SP appeared well within the triangular space spanned by the relative fractions of *m/z* 43 vs. *m/z* 44, representing ambient organic aerosols from global AMS field studies (Ng et al. 2011), thus supporting its use as a surrogate for atmospherically processed combustion emissions. The difference in O/C between SOA_{NAP}-SP and $SOA_{\beta PIN}$-SP might be a consequence of the slightly higher photochemical age of the SOA_{NAP}-SP or differences in formation pathways, including the release of secondary VOCs from fragmentation. In contrast to the data from AMS measurements, for which correction procedures were developed to improve the accuracy of the derived elemental ratios (Canagaratna et al. 2015), in the data evaluation from the DIP measurement the peak at *m/z* 43.9898 of CO_2^+, which increases from, for example, thermal decarboxylation of carboxylic acids in the SOAs, is not considered because of a too high peak intensity from background air and the associated high uncertainty of the result. Consequently, the result of higher O/C for $SOA_{\beta PIN}$-SP than for SOA_{NAP}-SP could indicate a higher abundance of carboxylic groups in SOA_{NAP}-SP, represented by the AMS, but not by DIP, measurements. Future studies beyond the scope of this manuscript will discuss data from AMS and DIP in more detail.

It is possible that the aerosol's toxicity largely depends on the degree of oxidation induced by atmospheric aging. Thus, the hazards of functional groups of the detected organic compounds could have a decisive impact. Studies on PAHs, such as naphthalene, have demonstrated specific toxic effects on cells (IARC 2010), and these effects may be enhanced by their oxidized derivatives (Chowdhury et al. 2018). However, it has to be noted that this increased toxicity reflected specific oxidation stages and could change with oxidation mechanism given that studies have also shown a declined toxicity during aging for naphthalene (Han et al. 2020) or hydrocarbons (Jiang and Jang 2018). For selected terpenes emitted from coniferous plants, including also β-pinene, no adverse cytotoxic or genotoxic effects in A549 human lung cells were found in an ALI exposure study by Gminski et al. (2010), although mutagenic and carcinogenic effects were described for specific compounds such as α, β-unsaturated aldehydes and 2-octen (Gminski et al. 2010). In our study, there were similarities between the abundance of most functional groups and related compound classes in $SOA_{\beta PIN}$-SP and SOA_{NAP}-SP, such as furans, aldehydes, and ketones. The oxidation of naphthalene may lead to first-generation open-ring dicarbonyl products and closed-ring epoxide products (Wang et al. 2007). A recent *in vitro* proteome-wide study by Han et al. (2020) pointed out the importance of short-lived unsaturated carbonyls in aged naphthalene as the main toxic components at the posttranslational level. Furthermore, the oxidation of furan-containing compounds favored the formation of epoxides, which are associated with enhanced harmful cellular effects (Peterson 2013; Tăbăran et al. 2019). The intracellular oxidation of aldehyde groups by enzymes of the aldehyde dehydrogenase family has been associated with adverse effects on various cell types, especially concerning tumor initiation, metastasis, and therapeutic resistance (Ma and Allan 2011; Rebollido-Rios et al. 2020; Rodriguez-Torres and Allan 2016). Photooxidation of β-pinene resulted in nopinone as a major first-generation product, which in a second step may form nine-carbon multifunctional compounds (Sato et al. 2016). In contrast to aldehydes, ketones are less reactive and less electrophilic, characteristics that can be associated with lower toxicological effects. However, minor changes in the molecular structure could be decisive for adverse outcomes (LoPachin and Gavin 2014; Schwöbel et al. 2011). Future studies are warranted to evaluate the particle cellular uptake of the tested aerosols to better understand the bioaccessibility of specific chemical compositions and their cellular effects.

Our results indicate that the differential toxicity of the precursors [half maximal oral lethal dose (LD_{50}) (rat) naphthalene: 2,000 mg/m^3 (U.S. EPA 2021b); oral LD_{50} (rat) β-pinene: 5,000 mg/m^3 (U.S. EPA 2021a)] was retained after an equivalent photochemical age of 3 d. However, depending on particle size, altitude, and atmospheric compartment, the lifetime of a particle spans a range from a few hours up to 2 wk (Raes et al. 2000; Williams et al. 2002). From a chemical perspective, atmospheric aging increased the O/C ratio of any organic aerosol constituent toward the limit of 2 determined by CO_2, steadily increasing their functionalization (Kroll et al. 2011); yet AMS analysis of organic aerosol from the Northern Hemisphere did not exceed O/C ratios of 1.2 (Ng et al. 2010), also not for highly oxidized molecules (Ehn et al. 2014). Moreover, atmospheric aging involves several processes and conditions, such as distinct differences during day- and nighttime or ambient levels and distributions of nitrogen oxides (NO_x) species, triggering different reaction pathways. There is particularly strong evidence that exposure to nitrogen dioxide is associated with adverse effects on human health (Atkinson et al. 2018; Mills et al. 2015) and leads to the formation of atmospheric mutagens from PAHs (Atkinson and Arey 1994). However, the general role of NO_x in atmospheric aging on the toxicity of SOA is in the early stage of research (Chowdhury et al. 2019). Hence, it remains an unanswered question if, when, and how different structural properties of SOA precursors are influencing the chemical and toxicological properties of the respective SOA during photochemical aging.

The Importance of Using Mono- and Coculture Systems in Aerosol Studies

Although monocultures provide information on direct toxicological effects of nanomaterials, recent studies have pointed out that multicellular culture systems are important tools for modeling an *in vivo* physiological cellular environment, including the

interaction between different cell lines (Bengalli et al. 2013; Klein et al. 2013; Lacroix et al. 2018). It is well known that, apart from pulmonary adverse health effects, $PM_{2.5}$ can also induce an increased risk for cardiovascular morbidity and mortality (Brook et al. 2010). Dysfunction of endothelial cells in particular is suspected to play a major role in inducing cardiovascular injury after the inhalation of $PM_{2.5}$ in a cohort of healthy individuals (Pope et al. 2016), which highlights the importance of the used epithelial–endothelial coculture in our study to depict possible underlying mechanisms.

In our epithelial monoculture, SOA_{NAP}-SP induced a 10-fold higher, and $SOA_{\beta PIN}$-SP a 7-fold higher, release of LDH in the undiluted aerosol compared with CA controls. Interestingly, the relative difference in LDH was lower in our epithelial–endothelial coculture (5-fold) than in the monoculture after the exposure to both undiluted aerosols. It is conceivable that this effect was the result of an enhanced physical barrier due to the addition of endothelial cells on the basolateral side of the membrane. Notably, the diffusion of particle-related H_2O_2 content is presumed to represent a main pathway for inducing intracellular ROS formation (Liu et al. 2020). It was already shown that the SOA oxidative potential depends on the hydrocarbon precursor identity, with biogenic SOA having a lower water-soluble oxidative potential than anthropogenic SOA (Tuet et al. 2017). Indeed, we found a greater peroxide content in SOA_{NAP}-SP ($\sim$3.5 times higher compared with $SOA_{\beta PIN}$-SP) and a higher abundance of MDA ($\sim$2 times higher compared with $SOA_{\beta PIN}$-SP in the undiluted aerosol), which is an end product of the lipid peroxidation induced by free radicals (Ayala et al. 2014), in the cell culture medium of both mono- and cocultures. Assuming an enhanced physical barrier in the coculture system, but observing no differences in MDA release in the mono- and cocultures after the exposure to the tested SOAs, suggested an additional release of MDA from endothelial cells, possibly induced by oxidized phospholipids and cytotoxic compounds of the epithelial cells (Landar et al. 2006). Epidemiological and *in vivo* studies with $PM_{2.5}$ have identified inflammatory responses as a major adverse outcome pathway (Yan et al. 2016), and *in vitro* studies have highlighted the impact of endothelial cells in secreting pro-inflammatory mediators (Karki and Birukov 2020). In line with our observations of SOA_{NAP}-SP inducing cellular cytotoxicity and oxidative stress, we observed a greater release of IL-8 in the monoculture after the exposure to SOA_{NAP}-SP ($\approx$ 2-fold higher in the undiluted aerosol) compared with $SOA_{\beta PIN}$-SP (no difference in the undiluted aerosol). In addition, we showed higher secretion of IL-8 in the coculture compared with the monoculture system ($\approx$ 2-fold higher after the exposure to undiluted $SOA_{\beta PIN}$-SP and SOA_{NAP}-SP). Inflammation and oxidative stress are main drivers for the induction of DNA strand breaks (Møller et al. 2014). Consistent with our previous shown results on MDA and IL-8 release, we observed DNA breaks of $\approx 10\%$ for undiluted $SOA_{\beta PIN}$-SP and $\approx 16\,\%$ for undiluted SOA_{NAP}-SP in the monoculture. Moreover, experiments with conditioned media-based techniques revealed secondary genotoxic effects of nanomaterials (Åkerlund et al. 2019; Evans et al. 2019). To the best of our knowledge, this is the first study that showed secondary genotoxic effects on cells in a coculture system at ALI where a cell–cell interplay was provided. Here, we observed genotoxic effects on endothelial cells ($\approx 8\,\%$ DNA breaks) after the exposure with SOA_{NAP}-SP [undiluted (1:1) and 1:3 diluted] but not after $SOA_{\beta PIN}$-SP exposures. Further studies should investigate this observation to exclude a possible translocation of PM through the insert membrane and thus a direct effect on endothelial cells (Wang et al. 2019). However, the enhanced release of IL-8 in the coculture cell model compared with the monoculture following SOA_{NAP}-SP exposure, supported our assumption of secondary genotoxic effects given that cytokines may promote genomic instability and IL-8 is a pro-angiogenic factor, potentially explaining the observed cross-activation of endothelial cells (Aivaliotis et al. 2012; Heidemann et al. 2003). Furthermore, the angiogenesis assay with a conditioned media-based approach affirmed the cross-activation of endothelial cells after the exposure to SOA_{NAP}-SP. No difference in the angiogenic potential between the conditioned media of the mono- and cocultures was observed, indicating that besides IL-8 other pro-angiogenic factors and oxidative stress may also play a decisive role (Kim and Byzova 2014). The conditioned media of the coculture exposed to $SOA_{\beta PIN}$-SP induced a decreased angiogenic potential, whereas in the conditioned media of the monoculture, no difference from the control was detected. Future studies beyond the scope of this manuscript should investigate how $SOA_{\beta PIN}$-SP differently altered the angiogenic potential of endothelial cells in our experimental setup. In general, dysfunction of endothelial cells is associated with adverse health outcomes. Although a reduced angiogenic potential of endothelial cells after the inhalation of $PM_{2.5}$ has been observed in previous studies (Lan et al. 2020), and can be an indication for a compromised ventilation–perfusion ratio of the lung, an enhanced angiogenic potential is one of the hallmarks for several interstitial lung diseases (Ackermann et al. 2020).

Nonetheless, although coculture models are enhancing *in vitro* studies by including the interaction between cell types, to what extent this may reflect an *in vivo* physiological cellular environment is always of concern and further optimization and standardization are needed. For instance, although our coculture model focused on the deposition of inhaled $PM_{2.5}$ on epithelial cells, it is well accepted that resident immune cells are also directly targeted upon inhalation and thus, including immune competent cells would be an improvement of the model. Moreover, A549 cells at ALI are known to partially mimic the property of an alveolar epithelium (Wu et al. 2017a), but drawbacks include their low expression of tight junctions or adherence proteins and their inability to form a fully differentiated and polarized epithelium (Papazian et al. 2016). Therefore, the additional usage of different epithelial cells, which could represent a heterogeneous population of several different epithelial cell types, would have benefited our study. However, owing to the complexity of our experimental setup, we found with A549 a robust cell line that is suitable for large and repetitive studies. Further studies comparing simultaneous performed aerosol exposures *in vivo* with different *in vitro* cell culture systems should help to extrapolate within the framework of replacement, reduction, and refinement.

Conclusions

The ubiquitous layer of SOA components that condenses onto primary particles can have a strong impact on PM toxicity. In particular, SOA-coated combustion SPs showed higher toxicity compared with fresh combustion SPs. This emphasizes the importance of atmospheric transformations for the toxicity and adverse health effects of ambient aerosol particles and may help to explain the high numbers of air-pollution related mortality and morbidity cases identified by epidemiological studies. This study also demonstrated that different SOA precursors led to different toxicological outcomes at comparable exposure conditions. A typical anthropogenic, aromatic SOA precursor (naphthalene) mixed with SPs, led to condensation of higher oxidized, aromatic SOAs of higher oxidative potential on the SPs and induced stronger toxic effects in the investigated lung cell models. In contrast, a typical biogenic, aliphatic SOA precursor (β-pinene) led to condensation of less oxidized, aliphatic SOAs of lower oxidative potential on the SPs and induced milder toxic effects in the

investigated lung cell models. Our findings highlight the role of different structural–chemical properties of photochemically aged SOAs for *in vitro* toxicological outcomes. Moreover, we emphasize the importance of multicellular culture systems to model a normal physiological cell environment with intercellular crosstalk. Future studies will also focus on an in-depth characterization of the used aerosols and of aerosol-specific effects on transcriptomic and proteomic outcomes.

Acknowledgments

S.D.B., H.C., T.H., A.K.-S., Y.R. and R.Z. conceived and supervised the study. S.Ba., S.Bi., J.B., C.B., S.D.B., R.B., A.B., X.C., H.C., T.G., G.J., S.J., E.H, T.H., A.H., U.K., M.K., T.K., A.K.-S., E.K., P.M., A.Me, S.Oe, S.O., J.O., J.P., A.P., N.R., Y.R., J.S.-K., O.S., M.S., Z.-H.Z., T.Z., E.J.Z. and R.Z. designed and performed the experiments. S.Ba., C.B., S.D.B., X.C., H.C., G.J., E.H, U.K., E.K., A.Ma, S.O., A.P., N.R. and M.S. analyzed and evaluated the data. A.K.-S., Y.R, and R.Z. provided funding; S.D.B., H.C., T.G., E.H, S.O., M.S. and R.Z. wrote the paper with input and approval from all the authors.

We thank the Helmholtz International Laboratory aeroHEALTH (InterLabs-0005; https://www.aerohealth.eu), the Helmholtz Association of German Research Centers and the Helmholtz Virtual Institute of Complex Systems in Environmental Health (InhaleHICE) for granting this project. Y.R. acknowledges support from the Estate of Raymond Lapon, the Estate of Betty Weneser, and Seed for Peace. Inc. C.B. acknowledges the support of the Swiss National Science Foundation (grant P2FRP3_178112). We also thank W.H. Brune (Pennsylvania State University) for providing the potential aerosol mass (PAM) reactor, which was funded by the University of Rostock.

References

Ackermann M, Stark H, Neubert L, Schubert S, Borchert P, Linz F, et al. 2020. Morphomolecular motifs of pulmonary neoangiogenesis in interstitial lung diseases. Eur Respir J 55(3):1900933, PMID: 31806721, https://doi.org/10.1183/13993003.00933-2019.

Aivaliotis IL, Pateras IS, Papaioannou M, Glytsou C, Kontzoglou K, Johnson EO, et al. 2012. How do cytokines trigger genomic instability? J Biomed Biotechnol 2012:536761, PMID: 22754280, https://doi.org/10.1155/2012/536761.

Åkerlund E, Islam MS, McCarrick S, Alfaro-Moreno E, Karlsson HL. 2019. Inflammation and (secondary) genotoxicity of Ni and NiO nanoparticles. Nanotoxicology 13(8):1060–1072, PMID: 31322448, https://doi.org/10.1080/17435390.2019.1640908.

Andreae MO, Gelencsér A. 2006. Black carbon or brown carbon? The nature of light-absorbing carbonaceous aerosols. Atmos Chem Phys 6(10):3131–3148, https://doi.org/10.5194/acp-6-3131-2006.

Aranda E, Owen GI. 2009. A semi-quantitative assay to screen for angiogenic compounds and compounds with angiogenic potential using the EA.hy926 endothelial cell line. Biol Res 42(3):377–389, PMID: 19915746, https://doi.org/10.4067/S0716-97602009000300012.

Arashiro M, Lin YH, Zhang Z, Sexton KG, Gold A, Jaspers I, et al. 2018. Effect of secondary organic aerosol from isoprene-derived hydroxyhydroperoxides on the expression of oxidative stress response genes in human bronchial epithelial cells. Environ Sci Process Impacts 20(2):332–339, PMID: 29292423, https://doi.org/10.1039/c7em00439g.

Atkinson R, Arey J. 1994. Atmospheric chemistry of gas-phase polycyclic aromatic hydrocarbons: formation of atmospheric mutagens. Environ Health Perspect 102(suppl 4):117–126, PMID: 7821285, https://doi.org/10.1289/ehp.94102s4117.

Atkinson R, Arey J. 2003. Atmospheric degradation of volatile organic compounds. Chem Rev 103(12):4605–4638, PMID: 14664626, https://doi.org/10.1021/cr0206420.

Atkinson RW, Butland BK, Anderson HR, Maynard RL. 2018. Long-term concentrations of nitrogen dioxide and mortality: a meta-analysis of cohort studies. Epidemiology 29(4):460–472, PMID: 29746370, https://doi.org/10.1097/EDE.0000000000000847.

Atkinson R, Carter WPL. 1984. Kinetics and mechanisms of the gas-phase reactions of ozone with organic compounds under atmospheric conditions. Chem Rev 84(5):437–470, https://doi.org/10.1021/cr00063a002.

Ayala A, Muñoz MF, Argüelles S. 2014. Lipid peroxidation: production, metabolism, and signaling mechanisms of malondialdehyde and 4-hydroxy-2-nonenal. Oxid Med Cell Longev 2014:360438, PMID: 24999379, https://doi.org/10.1155/2014/360438.

Barmet P, Dommen J, DeCarlo PF, Tritscher T, Praplan AP, Platt SM, et al. 2012. OH clock determination by proton transfer reaction mass spectrometry at an environmental chamber. Atmos Meas Tech 5(3):647–656, https://doi.org/10.5194/amt-5-647-2012.

Barosova H, Meldrum K, Karakocak BB, Balog S, Doak SH, Petri-Fink A, et al. 2021. Inter-laboratory variability of A549 epithelial cells grown under submerged and air-liquid interface conditions. Toxicol In Vitro 75:105178, PMID: 33905840, https://doi.org/10.1016/j.tiv.2021.105178.

Bengalli R, Mantecca P, Camatini M, Gualtieri M. 2013. Effect of nanoparticles and environmental particles on a cocultures model of the air-blood barrier. Biomed Res Int 2013:801214, PMID: 23509780, https://doi.org/10.1155/2013/801214.

Bond TC, Doherty SJ, Fahey DW, Forster PM, Berntsen T, DeAngelo BJ, et al. 2013. Bounding the role of black carbon in the climate system: a scientific assessment. J Geophys Res Atmos 118(11):5380–5552, https://doi.org/10.1002/jgrd.50171.

Brook RD, Rajagopalan S, Pope CA III, Brook JR, Bhatnagar A, Diez-Roux AV, et al. 2010. Particulate matter air pollution and cardiovascular disease: an update to the scientific statement from the American Heart Association. Circulation 121(21):2331–2378, PMID: 20458016, https://doi.org/10.1161/CIR.0b013e3181dbece1.

Bruns EA, El Haddad I, Keller A, Klein F, Kumar NK, Pieber SM, et al. 2015. Inter-comparison of laboratory smog chamber and flow reactor systems on organic aerosol yield and composition. Atmos Meas Tech 8(6):2315–2332, https://doi.org/10.5194/amt-8-2315-2015.

Burkholder JB, Abbatt JPD, Barnes I, Roberts JM, Melamed ML, Ammann M, et al. 2017. The essential role for laboratory studies in atmospheric chemistry. Environ Sci Technol 51(5):2519–2528, PMID: 28169528, https://doi.org/10.1021/acs.est.6b04947.

Canagaratna MR, Jimenez JL, Kroll JH, Chen Q, Kessler SH, Massoli P, et al. 2015. Elemental ratio measurements of organic compounds using aerosol mass spectrometry: characterization, improved calibration, and implications. Atmos Chem Phys 15(1):253–272, https://doi.org/10.5194/acp-15-253-2015.

Chan AWH, Kautzman KE, Chhabra PS, Surratt JD, Chan MN, Crounse JD, et al. 2009. Secondary organic aerosol formation from photooxidation of naphthalene and alkylnaphthalenes: implications for oxidation of intermediate volatility organic compounds (IVOCs). Atmos Chem Phys 9(9):3049–3060, https://doi.org/10.5194/acp-9-3049-2009.

Chen CL, Kacarab M, Tang P, Cocker DR III. 2016. SOA formation from naphthalene, 1-methylnaphthalene, and 2-methylnaphthalene photooxidation. Atmos Environ 131:424–433, https://doi.org/10.1016/j.atmosenv.2016.02.007.

Chow JC, Watson JG, Chen LWA, Chang MCO, Robinson NF, Trimble D, et al. 2007. The IMPROVE_A temperature protocol for thermal/optical carbon analysis: maintaining consistency with a long-term database. J Air Waste Manag Assoc 57(9):1014–1023, PMID: 17912920, https://doi.org/10.3155/1047-3289.57.9.1014.

Chowdhury PH, He Q, Carmieli R, Li C, Rudich Y, Pardo M. 2019. Connecting the oxidative potential of secondary organic aerosols with reactive oxygen species in exposed lung cells. Environ Sci Technol 53(23):13949–13958, PMID: 31652049, https://doi.org/10.1021/acs.est.9b04449.

Chowdhury PH, He QF, Male TL, Brune WH, Rudich Y, Pardo M. 2018. Exposure of lung epithelial cells to photochemically aged secondary organic aerosol shows increased toxic effects. Environ Sci Technol Lett 5(7):424–430, https://doi.org/10.1021/acs.estlett.8b00256.

Chughtai AR, Kim JM, Smith DM. 2003. The effect of temperature and humidity on the reaction of ozone with combustion soot: implications for reactivity near the tropopause. J Atmos Chem 45(3):231–243, https://doi.org/10.1023/A:1024250505886.

Cohen AJ, Brauer M, Burnett R, Anderson HR, Frostad J, Estep K, et al. 2017. Estimates and 25-year trends of the global burden of disease attributable to ambient air pollution: an analysis of data from the Global Burden of Diseases Study 2015. Lancet 389(10082):1907–1918, PMID: 28408086, https://doi.org/10.1016/S0140-6736(17)30505-6.

DeCarlo PF, Kimmel JR, Trimborn A, Northway MJ, Jayne JT, Aiken AC, et al. 2006. Field-deployable, high-resolution, time-of-flight aerosol mass spectrometer. Anal Chem 78(24):8281–8289, PMID: 17165817, https://doi.org/10.1021/ac061249n.

Deng X, Zhang F, Rui W, Long F, Wang L, Feng Z, et al. 2013. $PM_{2.5}$-induced oxidative stress triggers autophagy in human lung epithelial A549 cells. Toxicol In Vitro 27(6):1762–1770, PMID: 23685237, https://doi.org/10.1016/j.tiv.2013.05.004.

Dennis-Smither BJ, Marshall FH, Miles REH, Preston TC, Reid JP. 2014. Volatility and oxidative aging of aqueous maleic acid aerosol droplets and the dependence on relative humidity. J Phys Chem A 118(30):5680–5691, PMID: 25003240, https://doi.org/10.1021/jp504823j.

Dergham M, Lepers C, Verdin A, Billet S, Cazier F, Courcot D, et al. 2012. Prooxidant and proinflammatory potency of air pollution particulate matter ($PM_{2.5–0.3}$) produced in rural, urban, or industrial surroundings in human bronchial epithelial cells (BEAS-2B). Chem Res Toxicol 25(4):904–919, PMID: 22404339, https://doi.org/10.1021/tx200529v.

Di Bucchianico S, Cappellini F, Le Bihanic F, Zhang Y, Dreij K, Karlsson HL. 2017. Genotoxicity of TiO_2 nanoparticles assessed by mini-gel comet assay and micronucleus scoring with flow cytometry. Mutagenesis 32(1):127–137, PMID: 27382040, https://doi.org/10.1093/mutage/gew030.

Drwal E, Rak A, Gregoraszczuk EL. 2019. Review: polycyclic aromatic hydrocarbons (PAHs)—action on placental function and health risks in future life of newborns. Toxicology 411:133–142, PMID: 30321648, https://doi.org/10.1016/j.tox.2018.10.003.

Eaves LA, Smeester L, Hartwell HJ, Lin YH, Arashiro M, Zhang Z, et al. 2020. Isoprene-derived secondary organic aerosol induces the expression of microRNAs associated with inflammatory/oxidative stress response in lung cells. Chem Res Toxicol 33(2):381–387, PMID: 31765140, https://doi.org/10.1021/acs.chemrestox.9b00322.

Ehn M, Thornton JA, Kleist E, Sipilä M, Junninen H, Pullinen I, et al. 2014. A large source of low-volatility secondary organic aerosol. Nature 506(7489):476–479, PMID: 24572423, https://doi.org/10.1038/nature13032.

Evans SJ, Clift MJD, Singh N, Wills JW, Hondow N, Wilkinson TS, et al. 2019. In vitro detection of in vitro secondary mechanisms of genotoxicity induced by engineered nanomaterials. Part Fibre Toxicol 16(1):8, PMID: 30760282, https://doi.org/10.1186/s12989-019-0291-7.

Faiola CL, Jobson BT, VanReken TM. 2015. Impacts of simulated herbivory on volatile organic compound emission profiles from coniferous plants. Biogeosciences 12(2):527–547, https://doi.org/10.5194/bg-12-527-2015.

Feng S, Gao D, Liao F, Zhou F, Wang X. 2016. The health effects of ambient $PM_{2.5}$ and potential mechanisms. Ecotoxicol Environ Saf 128:67–74, PMID: 26896893, https://doi.org/10.1016/j.ecoenv.2016.01.030.

Gaspari L, Chang SS, Santella RM, Garte S, Pedotti P, Taioli E. 2003. Polycyclic aromatic hydrocarbon-DNA adducts in human sperm as a marker of DNA damage and infertility. Mutat Res 535(2):155–160, PMID: 12581533, https://doi.org/10.1016/S1383-5718(02)00297-8.

Gminski R, Tang T, Mersch-Sundermann V. 2010. Cytotoxicity and genotoxicity in human lung epithelial A549 cells caused by airborne volatile organic compounds emitted from pine wood and oriented strand boards. Toxicol Lett 196(1):33–41, PMID: 20362040, https://doi.org/10.1016/j.toxlet.2010.03.015.

Guenther A, Hewitt CN, Erickson D, Fall R, Geron C, Graedel T, et al. 1995. A global model of natural volatile organic compound emissions. J Geophys Res 100(D5):8873–8892, https://doi.org/10.1029/94JD02950.

Guenther AB, Jiang X, Heald CL, Sakulyanontvittaya T, Duhl T, Emmons LK, et al. 2012. The Model of Emissions of Gases and Aerosols from Nature version 2.1 (MEGAN2.1): an extended and updated framework for modeling biogenic emissions. Geosci Model Dev 5(6):1471–1492, https://doi.org/10.5194/gmd-5-1471-2012.

Halappanavar S, van den Brule S, Nymark P, Gaté L, Seidel C, Valentino S, et al. 2020. Adverse outcome pathways as a tool for the design of testing strategies to support the safety assessment of emerging advanced materials at the nanoscale. Part Fibre Toxicol 17(1):16, PMID: 32450889, https://doi.org/10.1186/s12989-020-00344-4.

Hallquist M, Wenger JC, Baltensperger U, Rudich Y, Simpson D, Claeys M, et al. 2009. The formation, properties and impact of secondary organic aerosol: current and emerging issues. Atmos Chem Phys 9(14):5155–5236, https://doi.org/10.5194/acp-9-5155-2009.

Han J, Wang S, Yeung K, Yang D, Gu W, Ma Z, et al. 2020. Proteome-wide effects of naphthalene-derived secondary organic aerosol in BEAS-2B cells are caused by short-lived unsaturated carbonyls. Proc Natl Acad Sci U S A 117(41):25386–25395, PMID: 32989125, https://doi.org/10.1073/pnas.2001378117.

Hartikainen A, Tiitta P, Ihalainen M, Yli-Pirilä P, Orasche J, Czech H, et al. 2020. Photochemical transformation of residential wood combustion emissions: dependence of organic aerosol composition on OH exposure. Atmos Chem Phys 20(11):6357–6378, https://doi.org/10.5194/acp-20-6357-2020.

Heidemann J, Ogawa H, Dwinell MB, Rafiee P, Maaser C, Gockel HR, et al. 2003. Angiogenic effects of interleukin 8 (CXCL8) in human intestinal microvascular endothelial cells are mediated by CXCR2. J Biol Chem 278(10):8508–8515, PMID: 12496258, https://doi.org/10.1074/jbc.M208231200.

Heyder J. 2004. Deposition of inhaled particles in the human respiratory tract and consequences for regional targeting in respiratory drug delivery. Proc Am Thorac Soc 1(4):315–320, PMID: 16113452, https://doi.org/10.1513/pats.200409-046TA.

Hilton G, Barosova H, Petri-Fink A, Rothen-Rutishauser B, Bereman M. 2019. Leveraging proteomics to compare submerged versus air-liquid interface carbon nanotube exposure to a 3D lung cell model. Toxicol In Vitro 54:58–66, PMID: 30243732, https://doi.org/10.1016/j.tiv.2018.09.010.

Hohaus T, Gensch I, Kimmel J, Worsnop DR, Kiendler-Scharr A. 2015. Experimental determination of the partitioning coefficient of β-pinene oxidation products in SOAs. Phys Chem Phys 17(22):14796–14804, PMID: 25975709, https://doi.org/10.1039/c5cp01608h.

Huang RJ, Zhang Y, Bozzetti C, Ho KF, Cao JJ, Han Y, et al. 2014. High secondary aerosol contribution to particulate pollution during haze events in China. Nature 514(7521):218–222, PMID: 25231863, https://doi.org/10.1038/nature13774.

IARC (IARC Working Group on the Evaluation of Carcinogenic Risks to Humans). 2010. Some non-heterocyclic polycyclic aromatic hydrocarbons and some related exposures. IARC Monogr Eval Carcinog Risks Hum 92:1–853, PMID: 21141735.

Ihantola T, Di Bucchianico S, Happo M, Ihalainen M, Uski O, Bauer S, et al. 2020. Influence of wood species on toxicity of log-wood stove combustion aerosols: a parallel animal and air-liquid interface cell exposure study on spruce and pine smoke. Part Fibre Toxicol 17(1):27, PMID: 32539833, https://doi.org/10.1186/s12989-020-00355-1.

Janssen NAH, Hoek G, Simic-Lawson M, Fischer P, van Bree L, ten Brink H, et al. 2011. Black carbon as an additional indicator of the adverse health effects of airborne particles compared with PM_{10} and $PM_{2.5}$. Environ Health Perspect 119(12):1691–1699, PMID: 21810552, https://doi.org/10.1289/ehp.1003369.

Jayne JT, Leard DC, Zhang XF, Davidovits P, Smith KA, Kolb CE, et al. 2000. Development of an aerosol mass spectrometer for size and composition analysis of submicron particles. Aerosol Sci Technol 33(1–2):49–70, https://doi.org/10.1080/027868200410840.

Jia C, Batterman S. 2010. A critical review of naphthalene sources and exposures relevant to indoor and outdoor air. Int J Environ Res Public Health 7(7):2903–2939, PMID: 20717549, https://doi.org/10.3390/ijerph7072903.

Jiang H, Jang M. 2018. Dynamic oxidative potential of atmospheric organic aerosol under ambient sunlight. Environ Sci Technol 52(13):7496–7504, PMID: 29772167, https://doi.org/10.1021/acs.est.8b00148.

Käfer U, Gröger T, Rüger CP, Czech H, Saraji-Bozorgzad M, Wilharm T, et al. 2019. Direct inlet probe–high-resolution time-of-flight mass spectrometry as fast technique for the chemical description of complex high-boiling samples. Talanta 202:308–316, PMID: 31171187, https://doi.org/10.1016/j.talanta.2019.05.030.

Kaminski M, Fuchs H, Acir IH, Bohn B, Brauers T, Dorn HP, et al. 2017. Investigation of the β-pinene photooxidation by OH in the atmosphere simulation chamber SAPHIR. Atmos Chem Phys 17(11):6631–6650, https://doi.org/10.5194/acp-17-6631-2017.

Kang E, Root MJ, Toohey DW, Brune WH. 2007. Introducing the concept of potential aerosol mass (PAM). Atmos Chem Phys 7(22):5727–5744, https://doi.org/10.5194/acp-7-5727-2007.

Karg EW, Ferron GA, Bauer S, Di Bucchianico S, Zimmermann R. 2020. Is the particle deposition in a cell exposure facility comparable to the lungs? A computer model approach. Aerosol Sci Technol 54(6):668–684, https://doi.org/10.1080/02786826.2020.1724868.

Karki P, Birukov KG. 2020. Oxidized phospholipids in healthy and diseased lung endothelium. Cells 9(4):981, PMID: 32326516, https://doi.org/10.3390/cells9040981.

Kenseth CM, Huang Y, Zhao R, Dalleska NF, Hethcox JC, Stoltz BM, et al. 2018. Synergistic O_3 + OH oxidation pathway to extremely low-volatility dimers revealed in β-pinene secondary organic aerosol. Proc Natl Acad Sci U S A 115(33):8301–8306, PMID: 30076229, https://doi.org/10.1073/pnas.1804671115.

Keyte IJ, Harrison RM, Lammel G. 2013. Chemical reactivity and long-range transport potential of polycyclic aromatic hydrocarbons—a review. Chem Soc Rev 42(24):9333–9391, PMID: 24077263, https://doi.org/10.1039/c3cs60147a.

Kim YW, Byzova TV. 2014. Oxidative stress in angiogenesis and vascular disease. Blood 123(5):625–631, PMID: 24300855, https://doi.org/10.1182/blood-2013-09-512749.

Klein SG, Serchi T, Hoffmann L, Blömeke B, Gutleb AC. 2013. An improved 3D tetraculture system mimicking the cellular organisation at the alveolar barrier to study the potential toxic effects of particles on the lung. Part Fibre Toxicol 10:31, PMID: 23890538, https://doi.org/10.1186/1743-8977-10-31.

Kleist E, Mentel TF, Andres S, Bohne A, Folkers A, Kiendler-Scharr A, et al. 2012. Irreversible impacts of heat on the emissions of monoterpenes, sesquiterpenes, phenolic BVOC and green leaf volatiles from several tree species. Biogeosciences 9(12):5111–5123, https://doi.org/10.5194/bg-9-5111-2012.

Kouassi KS, Billet S, Garçon G, Verdin A, Diouf A, Cazier F, et al. 2010. Oxidative damage induced in A549 cells by physically and chemically characterized air particulate matter ($PM_{2.5}$) collected in Abidjan, Côte D'Ivoire. J Appl Toxicol 30(4):310–320, PMID: 19943358, https://doi.org/10.1002/jat.1496.

Kroll JH, Donahue NM, Jimenez JL, Kessler SH, Canagaratna MR, Wilson KR, et al. 2011. Carbon oxidation state as a metric for describing the chemistry of atmospheric organic aerosol. Nat Chem 3(2):133–139, PMID: 21258386, https://doi.org/10.1038/nchem.948.

Künzi L, Krapf M, Daher N, Dommen J, Jeannet N, Schneider S, et al. 2015. Toxicity of aged gasoline exhaust particles to normal and diseased airway epithelia. Sci Rep 5:11801, PMID: 26119831, https://doi.org/10.1038/srep11801.

Lacroix G, Koch W, Ritter D, Gutleb AC, Larsen ST, Loret T, et al. 2018. Air–liquid interface *in vitro* models for respiratory toxicology research: consensus workshop and recommendations. Appl In Vitro Toxicol 4(2):91–106, PMID: 32953944, https://doi.org/10.1089/aivt.2017.0034.

Låg M, Øvrevik J, Refsnes M, Holme JA. 2020. Potential role of polycyclic aromatic hydrocarbons in air pollution-induced non-malignant respiratory diseases. Respir Res 21(1):299, PMID: 33187512, https://doi.org/10.1186/s12931-020-01563-1.

Lan Y, Ng CT, Ong RXS, Muniasamy U, Baeg GH, Ong CN, et al. 2020. Urban $PM_{2.5}$ reduces angiogenic ability of endothelial cells in an alveolar-capillary co-culture lung model. Ecotoxicol Environ Saf 202:110932, PMID: 32800216, https://doi.org/10.1016/j.ecoenv.2020.110932.

Landar A, Zmijewski JW, Dickinson DA, Le Goffe C, Johnson MS, Milne GL, et al. 2006. Interaction of electrophilic lipid oxidation products with mitochondria in endothelial cells and formation of reactive oxygen species. Am J Physiol Heart Circ Physiol 290(5):H1777–H1787, PMID: 16387790, https://doi.org/10.1152/ajpheart.01087.2005.

Lenz AG, Karg E, Brendel E, Hinze-Heyn H, Maier KL, Eickelberg O, et al. 2013. Inflammatory and oxidative stress responses of an alveolar epithelial cell line to airborne zinc oxide nanoparticles at the air-liquid interface: a comparison with conventional, submerged cell-culture conditions. Biomed Res Int 2013:652632, PMID: 23484138, https://doi.org/10.1155/2013/652632.

Li D, Li Y, Li G, Zhang Y, Li J, Chen H. 2019. Fluorescent reconstitution on deposition of $PM_{2.5}$ in lung and extrapulmonary organs. Proc Natl Acad Sci U S A 116(7):2488–2493, PMID: 30692265, https://doi.org/10.1073/pnas.1818134116.

Lim CY, Browne EC, Sugrue RA, Kroll JH. 2017. Rapid heterogeneous oxidation of organic coatings on submicron aerosols. Geophys Res Lett 44(6):2949–2957, https://doi.org/10.1002/2017GL072585.

Lin YH, Arashiro M, Clapp PW, Cui T, Sexton KG, Vizuete W, et al. 2017. Gene expression profiling in human lung cells exposed to isoprene-derived secondary organic aerosol. Environ Sci Technol 51(14):8166–8175, PMID: 28636383, https://doi.org/10.1021/acs.est.7b01967.

Liu F, Saavedra MG, Champion JA, Griendling KK, Ng NL. 2020. Prominent contribution of hydrogen peroxide to intracellular reactive oxygen species generated upon exposure to naphthalene secondary organic aerosols. Environ Sci Technol Lett 7(3):171–177, https://doi.org/10.1021/acs.estlett.9b00773.

Löndahl J, Möller W, Pagels JH, Kreyling WG, Swietlicki E, Schmid O. 2014. Measurement techniques for respiratory tract deposition of airborne nanoparticles: a critical review. J Aerosol Med Pulm Drug Deliv 27(4):229–254, PMID: 24151837, https://doi.org/10.1089/jamp.2013.1044.

Longhin E, Holme JA, Gutzkow KB, Arlt VM, Kucab JE, Camatini M, et al. 2013. Cell cycle alterations induced by urban PM2.5 in bronchial epithelial cells: characterization of the process and possible mechanisms involved. Part Fibre Toxicol 10:63, PMID: 24354623, https://doi.org/10.1186/1743-8977-10-63.

LoPachin RM, Gavin T. 2014. Molecular mechanisms of aldehyde toxicity: a chemical perspective. Chem Res Toxicol 27(7):1081–1091, PMID: 24911545, https://doi.org/10.1021/tx5001046.

Loret T, Peyret E, Dubreuil M, Aguerre-Chariol O, Bressot C, le Bihan O, et al. 2016. Air-liquid interface exposure to aerosols of poorly soluble nanomaterials induces different biological activation levels compared to exposure to suspensions. Part Fibre Toxicol 13(1):58, PMID: 27919268, https://doi.org/10.1186/s12989-016-0171-3.

Lucci F, Castro ND, Rostami AA, Oldham MJ, Hoeng J, Pithawalla YB, et al. 2018. Characterization and modeling of aerosol deposition in Vitrocell ® exposure systems—exposure well chamber deposition efficiency. J Aerosol Sci 123:141–160, https://doi.org/10.1016/j.jaerosci.2018.06.015.

Ma I, Allan AL. 2011. The role of human aldehyde dehydrogenase in normal and cancer stem cells. Stem Cell Rev Rep 7(2):292–306, PMID: 21103958, https://doi.org/10.1007/s12015-010-9208-4.

Mills IC, Atkinson RW, Kang S, Walton H, Anderson HR. 2015. Quantitative systematic review of the associations between short-term exposure to nitrogen dioxide and mortality and hospital admissions. BMJ Open 5(5):e006946, PMID: 25967992, https://doi.org/10.1136/bmjopen-2014-006946.

Møller P, Danielsen PH, Karottki DG, Jantzen K, Roursgaard M, Klingberg H, et al. 2014. Oxidative stress and inflammation generated DNA damage by exposure to air pollution particles. Mutat Res Rev Mutat Res 762:133–166, PMID: 25475422, https://doi.org/10.1016/j.mrrev.2014.09.001.

Moore RH, Ziemba LD, Dutcher D, Beyersdorf AJ, Chan K, Crumeyrolle S, et al. 2014. Mapping the operation of the miniature combustion aerosol standard (Mini-CAST) soot generator. Aerosol Sci Technol 48(5):467–479, https://doi.org/10.1080/02786826.2014.890694.

Mülhopt S, Dilger M, Diabaté S, Schlager C, Krebs T, Zimmermann R, et al. 2016. Toxicity testing of combustion aerosols at the air–liquid interface with a self-contained and easy-to-use exposure system. J Aerosol Sci 96:38–55, https://doi.org/10.1016/j.jaerosci.2016.02.005.

National Academies of Sciences, Engineering, and Medicine. 2016. *The Future of Atmospheric Chemistry Research: Remembering Yesterday, Understanding Today, Anticipating Tomorrow*. Washington, DC: National Academies Press.

Ng NL, Canagaratna MR, Jimenez JL, Chhabra PS, Seinfeld JH, Worsnop DR. 2011. Changes in organic aerosol composition with aging inferred from aerosol mass spectra. Atmos Chem Phys 11(13):6465–6474, https://doi.org/10.5194/acp-11-6465-2011.

Ng NL, Canagaratna MR, Zhang Q, Jimenez JL, Tian J, Ulbrich IM, et al. 2010. Organic aerosol components observed in Northern Hemispheric datasets from Aerosol Mass Spectrometry. Atmos Chem Phys 10(10):4625–4641, https://doi.org/10.5194/acp-10-4625-2010.

Oeder S, Kanashova T, Sippula O, Sapcariu SC, Streibel T, Arteaga-Salas JM, et al. 2015. Particulate matter from both heavy fuel oil and diesel fuel shipping emissions show strong biological effects on human lung cells at realistic and comparable *in vitro* exposure conditions. PLoS One 10(6):e0126536, PMID: 26039251, https://doi.org/10.1371/journal.pone.0126536.

Papazian D, Würtzen PA, Hansen SWK. 2016. Polarized airway epithelial models for immunological co-culture studies. Int Arch Allergy Immunol 170(1):1–21, PMID: 27240620, https://doi.org/10.1159/000445833.

Park M, Joo HS, Lee K, Jang M, Kim SD, Kim I, et al. 2018. Differential toxicities of fine particulate matters from various sources. Sci Rep 8(1):17007, PMID: 30451941, https://doi.org/10.1038/s41598-018-35398-0.

Paur HR, Cassee FR, Teeguarden J, Fissan H, Diabate S, Aufderheide M, et al. 2011. In-vitro cell exposure studies for the assessment of nanoparticle toxicity in the lung—a dialog between aerosol science and biology. J Aerosol Sci 42(10):668–692, https://doi.org/10.1016/j.jaerosci.2011.06.005.

Peng Z, Day DA, Ortega AM, Palm BB, Hu W, Stark H, et al. 2016. Non-OH chemistry in oxidation flow reactors for the study of atmospheric chemistry systematically examined by modeling. Atmos Chem Phys 16(7):4283–4305, https://doi.org/10.5194/acp-16-4283-2016.

Perera F, Hemminki K, Jedrychowski W, Whyatt R, Campbell U, Hsu Y, et al. 2002. *In utero* DNA damage from environmental pollution is associated with somatic gene mutation in newborns. Cancer Epidemiol Biomark Prev 11(10 pt 1):1134–1137, PMID: 12376523.

Peters A, Nawrot TS, Baccarelli AA. 2021. Hallmarks of environmental insults. Cell 184(6):1455–1468, PMID: 33657411, https://doi.org/10.1016/j.cell.2021.01.043.

Peterson LA. 2013. Reactive metabolites in the biotransformation of molecules containing a furan ring. Chem Res Toxicol 26(1):6–25, PMID: 23061605, https://doi.org/10.1021/tx3003824.

Pieber SM, Kumar NK, Klein F, Comte P, Bhattu D, Dommen J, et al. 2018. Gas-phase composition and secondary organic aerosol formation from standard and particle filter-retrofitted gasoline direct injection vehicles investigated in a batch and flow reactor. Atmos Chem Phys 18(13):9929–9954, https://doi.org/10.5194/acp-18-9929-2018.

Pope CA III, Bhatnagar A, McCracken JP, Abplanalp W, Conklin DJ, O'Toole T. 2016. Exposure to fine particulate air pollution is associated with endothelial injury and systemic inflammation. Circ Res 119(11):1204–1214, PMID: 27780829, https://doi.org/10.1161/CIRCRESAHA.116.309279.

Pope CA III, Coleman N, Pond ZA, Burnett RT. 2020. Fine particulate air pollution and human mortality: 25+ years of cohort studies. Environ Res 183:108924, PMID: 31831155, https://doi.org/10.1016/j.envres.2019.108924.

Prinn RG, Huang J, Weiss RF, Cunnold DM, Fraser PJ, Simmonds PG, et al. 2001. Evidence for substantial variations of atmospheric hydroxyl radicals in the past two decades. Science 292(5523):1882–1888, PMID: 11337586, https://doi.org/10.1126/science.1058673.

Qian Z, Chen Y, Liu Z, Han Y, Zhang Y, Feng Y, et al. 2021. Intermediate volatile organic compound emissions from residential solid fuel combustion based on field measurements in rural China. Environ Sci Technol 55(9):5689–5700, PMID: 33797233, https://doi.org/10.1021/acs.est.0c07908.

Raes F, Van Dingenen R, Vignati E, Wilson J, Putaud JP, Seinfeld JH, et al. 2000. Formation and cycling of aerosols in the global troposphere. Atmos Environ 34(25):4215–4240, https://doi.org/10.1016/S1352-2310(00)00239-9.

Rebollido-Rios R, Venton G, Sánchez-Redondo S, Iglesias I Felip C, Fournet G, González E, et al. 2020. Dual disruption of aldehyde dehydrogenases 1 and 3 promotes functional changes in the glutathione redox system and enhances chemosensitivity in nonsmall cell lung cancer. Oncogene 39(13):2756–2771, PMID: 32015486, https://doi.org/10.1038/s41388-020-1184-9.

Riediker M, Zink D, Kreyling W, Oberdörster G, Elder A, Graham U, et al. 2019. Particle toxicology and health—where are we? Part Fibre Toxicol 16(1):19, PMID: 31014371, https://doi.org/10.1186/s12989-019-0302-8.

Rodriguez-Torres M, Allan AL. 2016. Aldehyde dehydrogenase as a marker and functional mediator of metastasis in solid tumors. Clin Exp Metastasis 33(1):97–113, PMID: 26445849, https://doi.org/10.1007/s10585-015-9755-9.

Rothen-Rutishauser B, Blank F, Mühlfeld C, Gehr P. 2008. *In vitro* models of the human epithelial airway barrier to study the toxic potential of particulate matter. Expert Opin Drug Metab Toxicol 4(8):1075–1089, PMID: 18680442, https://doi.org/10.1517/17425255.4.8.1075.

Sarrafzadeh M, Wildt J, Pullinen I, Springer M, Kleist E, Tillmann R, et al. 2016. Impact of NO*x* and OH on secondary organic aerosol formation from β-pinene photooxidation. Atmos Chem Phys 16(17):11237–11248, https://doi.org/10.5194/acp-16-11237-2016.

Sato K, Jia T, Tanabe K, Morino Y, Kajii Y, Imamura T. 2016. Terpenylic acid and nine-carbon multifunctional compounds formed during the aging of β-pinene ozonolysis secondary organic aerosol. Atmos Environ 130:127–135, https://doi.org/10.1016/j.atmosenv.2015.08.047.

Schwöbel JAH, Koleva YK, Enoch SJ, Bajot F, Hewitt M, Madden JC, et al. 2011. Measurement and estimation of electrophilic reactivity for predictive toxicology. Chem Rev 111(4):2562–2596, PMID: 21401043, https://doi.org/10.1021/cr100098n.

Shakya KM, Griffin RJ. 2010. Secondary organic aerosol from photooxidation of polycyclic aromatic hydrocarbons. Environ Sci Technol 44(21):8134–8139, PMID: 20919733, https://doi.org/10.1021/es1019417.

Sýkorová B, Kucbel M, Raclavský K. 2016. Composition of airborne particulate matter in the industrial area versus mountain area. Perspect Sci (Neth) 7:369–372, https://doi.org/10.1016/j.pisc.2015.12.006.

Tăbăran AF, O'Sullivan MG, Seabloom DE, Vevang KR, Smith WE, Wiedmann TS, et al. 2019. Inhaled furan selectively damages club cells in lungs of A/J mice. Toxicol Pathol 47(7):842–850, PMID: 31426723, https://doi.org/10.1177/0192623319869306.

Tuet WY, Chen YL, Xu L, Fok S, Gao D, Weber RJ, et al. 2017. Chemical oxidative potential of secondary organic aerosol (SOA) generated from the photooxidation of biogenic and anthropogenic volatile organic compounds. Atmos Chem Phys 17(2):839–853, https://doi.org/10.5194/acp-17-839-2017.

U.S. EPA (Environmental Protection Agency). 2021a. EPA CompTox Chemicals Dashboard: Beta-pinene. https://comptox.epa.gov/dashboard/dsstoxdb/results?search=beta-pinene#toxicity-values [accessed 3 December 2021].

U.S. EPA. 2021b. EPA CompTox Chemicals Dashboard: Naphthalene. https://comptox.epa.gov/dashboard/dsstoxdb/results?search=DTXSID8020913#toxicity-values [accessed 3 December 2021].

Wang G, Zhang X, Liu X, Zheng J, Chen R, Kan H. 2019. Ambient fine particulate matter induce toxicity in lung epithelial-endothelial co-culture models. Toxicol Lett 301:133–145, PMID: 30481584, https://doi.org/10.1016/j.toxlet.2018.11.010.

Wang L, Atkinson R, Arey J. 2007. Dicarbonyl products of the OH radical-initiated reactions of naphthalene and the C_1- and C_2-alkylnaphthalenes. Environ Sci Technol 41(8):2803–2810, PMID: 17533842, https://doi.org/10.1021/es0628102.

Wang M, Li S, Zhu R, Zhang R, Zu L, Wang Y, et al. 2020. On-road tailpipe emission characteristics and ozone formation potentials of VOCs from gasoline, diesel and liquefied petroleum gas fueled vehicles. Atmos Environ 223:117294, https://doi.org/10.1016/j.atmosenv.2020.117294.

Watne ÅK, Westerlund J, Hallquist ÅM, Brune WH, Hallquist M. 2017. Ozone and OH-induced oxidation of monoterpenes: changes in the thermal properties of secondary organic aerosol (SOA). J Aerosol Sci 114:31–41, https://doi.org/10.1016/j.jaerosci.2017.08.011.

Weitekamp CA, Stevens T, Stewart MJ, Bhave P, Gilmour MI. 2020. Health effects from freshly emitted versus oxidatively or photochemically aged air pollutants. Sci Total Environ 704:135772, PMID: 31838301, https://doi.org/10.1016/j.scitotenv.2019.135772.

Welch BL. 1947. The generalisation of 'Student's' problems when several different population variances are involved. Biometrika 34(1–2):28–35, PMID: 20287819, https://doi.org/10.2307/2332510.

Williams BJ, Goldstein AH, Kreisberg NM, Hering SV. 2010. *In situ* measurements of gas/particle-phase transitions for atmospheric semivolatile organic compounds. Proc Natl Acad Sci USA 107(15):6676–6681, PMID: 20142511, https://doi.org/10.1073/pnas.0911858107.

Williams J, de Reus M, Krejci R, Fischer H, Ström J. 2002. Application of the variability-size relationship to atmospheric aerosol studies: estimating aerosol lifetimes and ages. Atmos Chem Phys 2(2):133–145, https://doi.org/10.5194/acp-2-133-2002.

Wragg FPH, Fuller SJ, Freshwater R, Green DC, Kelly FJ, Kalberer M. 2016. An automated online instrument to quantify aerosol-bound reactive oxygen species (ROS) for ambient measurement and health-relevant aerosol studies. Atmos Meas Tech 9(10):4891–4900, https://doi.org/10.5194/amt-9-4891-2016.

Wu J, Wang Y, Liu G, Jia Y, Yang J, Shi J, et al. 2017a. Characterization of air-liquid interface culture of A549 alveolar epithelial cells. Braz J Med Biol Res 51(2):e6950, PMID: 29267508, https://doi.org/10.1590/1414-431X20176950.

Wu X, Lintelmann J, Klingbeil S, Li J, Wang H, Kuhn E, et al. 2017b. Determination of air pollution-related biomarkers of exposure in urine of travellers between Germany and China using liquid chromatographic and liquid chromatographic-mass spectrometric methods: a pilot study. Biomarkers 22(6):525–536, PMID: 28330376, https://doi.org/10.1080/1354750X.2017.1306753.

Wyzga RE, Rohr AC. 2015. Long-term particulate matter exposure: attributing health effects to individual PM components. J Air Waste Manag Assoc 65(5):523–543, PMID: 25947312, https://doi.org/10.1080/10962247.2015.1020396.

Xavier C, Rusanen A, Zhou PT, Dean C, Pichelstorfer L, Roldin P, et al. 2019. Aerosol mass yields of selected biogenic volatile organic compounds—a theoretical study with nearly explicit gas-phase chemistry. Atmos Chem Phys 19(22):13741–13758, https://doi.org/10.5194/acp-19-13741-2019.

Xu J, Hu W, Liang D, Gao P. 2022. Photochemical impacts on the toxicity of $PM_{2.5}$. Crit Rev Environ Sci Technol 52(1):130–156, https://doi.org/10.1080/10643389.2020.1816126.

Yan Z, Jin Y, An Z, Liu Y, Samet JM, Wu W. 2016. Inflammatory cell signaling following exposures to particulate matter and ozone. Biochim Biophys Acta 1860(12):2826–2834, PMID: 27015762, https://doi.org/10.1016/j.bbagen.2016.03.030.